PHYSICAL REVIEW FLUIDS **4**, 034605 (2019)

Streamline segment statistics propagation in inhomogeneous turbulence

A. Rubbert[*] and M. Albers
Chair of Fluid Mechanics and Institute of Aerodynamics Aachen,
RWTH Aachen University, Wüllnerstraße 5a, 52062 Aachen, Germany

W. Schröder
Chair of Fluid Mechanics and Institute of Aerodynamics Aachen,
RWTH Aachen University, Wüllnerstraße 5a, 52062 Aachen, Germany
and Forschungszentrum Jülich, JARA High-Performance Computing,
Wilhelm-Johnen-Straße, Jülich 52425, Germany

(Received 9 August 2018; published 25 March 2019)

The streamline segmentation method proposed by Wang is applied to a turbulent wavy channel flow to investigate the impact of pressure-driven strain on the streamline segment probability distribution. While the asymmetrical shape of the probability distribution is known to react to streamwise strains, in regions of detached flow this impact is severely less pronounced. Using tomographic particle-image velocimetry measurements and numerical data in attached and detached flow, the origin for this observation is found in the strong compressive strain during attached flow. The responsible mechanism is determined by introducing a concept of streamline segment locality, adapting the propagation equation for streamline segment statistics to inhomogeneous flow and applying it to the numerical data. A locally increased segment cutting rate is identified to cause the reduced sensitivity of the segment probability distribution to the local strain.

DOI: 10.1103/PhysRevFluids.4.034605

I. INTRODUCTION

Flows in engineering applications are predominantly turbulent, which has caused continued interest in the research community for more than a century. While it is generally accepted that turbulent flows are described by the Navier-Stokes equations [1], their direct numerical solution will remain computationally infeasible for the majority of engineering problems for the foreseeable future due to the wide range of nonlinearly interacting spatial and temporal scales. Because of the enormous complexity and the high sensitivity toward initial conditions, turbulent flows have traditionally been described as random processes that can be investigated by statistical means. Tritton [2], however, notes that the seemingly random behavior must contain structures, as a completely random behavior would render any definition of turbulence pointless.

An abundance of structures has been proposed as possible candidates to mitigate the difficulties describing turbulent flows. Corrsin [3] tried to identify "naturally identifiable" geometries appearing in turbulent flows. The decomposition of turbulent flows into various type zones presenting specific characteristics was proposed by Hunt *et al.* [4]. Traditionally, vortices or eddies have been the corner stone of turbulence descriptions ranging from Richardson's energy cascade [5] to current vortex tube analyses [1], suggesting vortex stretching as the main mechanism to transfer kinetic energy from large to small scales. While there has been extensive research into vortex dynamics, even the

---

[*] a.rubbert@aia.rwth-aachen.de

definition of what constitutes a vortex is generally ambiguous with multiple established criteria currently in use, as summarized by Haller [6]. Additionally, Ruetsch and Maxey [7] report that approximately half of the dissipation occurs in regions not associated with vortex tubes such that the suitability of a turbulence model solely based on vortex dynamics is to be questioned. Such doubts were also raised by Pullin and Saffman [8] citing the required free parameters, neglected inner vortex dynamics, and high levels of complexity by vortex tube models.

To address some of these shortcomings, Peters and Wang [9] proposed the dissipation element method to describe turbulent fields. The method partitions a scalar field into units which are called dissipation elements. Each element consists of all gradient trajectories connecting a particular pair of local extrema consisting of a local maximum and minimum in the base scalar field. Since every point of the field exhibits only one gradient, it is passed by exactly one gradient trajectory. Therefore, dissipation elements are not only space filling but furthermore unambiguously defined and nonoverlapping. Additionally, since they only span a region between local extrema, each dissipation element is strictly monotonous. As a consequence, turbulent behavior is not found within a single element. Rather, it is represented by the ensemble statistics of all elements. Typically, the resulting elements are parametrized by their length and their inner scalar difference. The likelihood of occurrence of a particular configuration of length and inner scalar difference is mapped in the joint probability distribution function (jPDF). The length distribution function is referred to as marginal PDF. Extensive studies have been conducted to develop a length distribution function [10] and to determine typical scaling behavior of dissipation elements [11]. Experimental investigations have substantiated these findings [12,13]. Additionally, the propagation equation has been used to predict model constants in a Reynolds-averaged Navier-Stokes turbulence model [14].

A related method is the streamline segmentation method proposed by Wang [15]. Instead of tracing gradient trajectories of an arbitrarily selected base scalar, streamlines are traced within the flow. The streamline is thereafter divided into segments based on local extrema of the absolute velocity. This approach preserves the flow's inherent topology as the streamline directionality is not lost, as it is when considering a scalar as the fundamental quantity for dissipation elements. In contrast to dissipation elements, it can be distinguished between accelerating streamline segments with positive velocity differences ($\Delta > 0$) and decelerating segments ($\Delta < 0$). As a result, accelerating segments will grow over time while decelerating segments will shrink in the absence of any other mechanism. In homogeneous turbulence, these inherent kinematics lead to a skewed, asymmetric probability distribution in which the mean segment length of all accelerating segments l_m^+ exceeds the mean segment length of decelerating segments l_m^- [15]. The close relation between dissipation elements and streamline segments is evidenced by their relation to the isosurface where the streamwise velocity gradients vanish. By definition, streamline segments begin and end on this surface. When the turbulent kinetic energy is chosen as the base scalar of dissipation elements, their constituent extremal points are located on the same surface.

In analogy to the dissipation element method, previous studies have developed a length distribution function [16], a scaling for the mean segment length [17], and a model function for the joint probability distribution function [18] of the segment length l and the inner velocity difference Δ for homogeneous shear, decaying, and forced turbulence. Current research is focused on the structure statistics in inhomogeneous flows. The findings for homogeneous flows were applied to experimental data obtained in a wavy channel flow and could largely be confirmed for multiple wave amplitudes and bulk Reynolds numbers [19]. By considering four small subvolumes near the wavy channel wall, the same study was able to show the effects of mean background strain due to the mean local acceleration on the asymmetry of the jPDF in inhomogeneous flows, which are omitted in the model function derived for homogeneous turbulence. The relation is presented in Fig. 1. However, in the region of the expansion slope and the trough of the wavy surface, i.e., in the varying pressure region, deviating behavior could be observed at low Reynolds numbers and a large wave amplitude. Under these conditions, a detached region is observed in the mean velocity field [20]. These deviating subvolumes are represented by the circle (o) and nabla (∇) symbols.

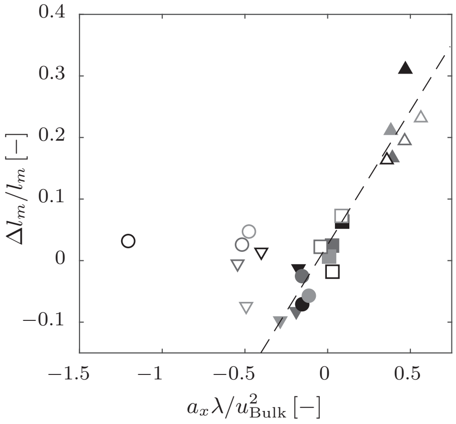

FIG. 1. Difference between positive and negative mean segment lengths depending on local flow acceleration for various positions in the wavy channel flow [19].

This study will further investigate the cause for the deviating behavior within and in the proximity of the expansion slope, when backflow events occur. Therefore, parameters yielding a distinct separation region in the mean flow field are chosen. Tomographic particle-image velocimetry (TPIV) measurements and numerical data are considered in the following analysis. The field of view is expanded in comparison to Ref. [19] to capture the entire expansion slope of the wavy wall. The acquisition of the experimental data and the postprocessing procedure are described in Sec. II A. The numerical method is presented in Sec. II B. The results are discussed in four steps starting with a comparison of the experimental and numerical results in Sec. III A. Whereas streamline segment statistics of all recorded samples were evaluated in Ref. [19], attached and detached flow conditions are considered separately in Sec. III B to understand the particular conditions in this region causing the asymmetry of the jPDF to become less sensitive to the background strain, in contrast to other regions of the flow. In particular, it is investigated whether large eruption events as observed in Ref. [21] cause the deviating behavior in the detached region. Schäfer *et al.* [18] propose the propagation equation for the probability distribution of streamline segments in homogeneous turbulence, which models various processes acting on the streamline segments. To identify the responsible mechanism for the locally deviating behavior, the propagation equation is reformulated for inhomogeneous flows in Sec. III C. An increased segment cutting rate is observed to decrease the statistical asymmetry of the jPDF since the occurrence rate of segment cutting events scales with the segment length. The newly derived propagation equation is applied to the obtained data in Sec. III D to obtain spatial distributions of this occurrence rate among other model parameters. Finally, the findings are summarized in Sec. IV.

II. DATA ACQUISITION AND PROCESSING

A. Experimental setup and data processing

All experiments were conducted in an Eiffel-type wind tunnel that provides a fully turbulent two-dimensional channel flow matching direct numerical simulation (DNS) results of Moser *et al.* [22] in the test section, which was verified in previous studies by Schäfer *et al.* [12]. The test section shown in Fig. 2 has an aspect ratio of 1:20 and measures $2h \times w = 100 \times 2\,000\,\mathrm{mm}^2$ (height × span) at a test section length of $\mathrm{l} = 2\ 500$ mm, i.e., $50h$ with the channel half-height h. The test section is optically accessible and is attached to a 9-m-long inlet section ($180h$) with two strips of sandpaper in the inlet to enforce laminar-turbulent transition. The test section possesses exchangeable sidewalls, allowing it to be equipped with various geometries. In the current study,

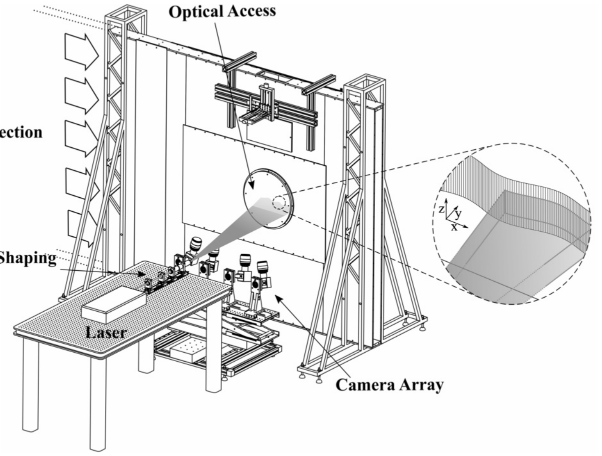

FIG. 2. Test section and tomographic PIV setup.

a sidewall with a sinusoidal shape, a wavelength of $2h = 100\,\mathrm{mm}$, and an amplitude of 5 mm, i.e., $0.1h$, was investigated for a bulk Reynolds number of 3 200 based on the bulk streamwise velocity $u_{\mathrm{Bulk}} = 1\,\mathrm{m/s}$ and the flat channel half-height h. The trough of the wave is aligned with the previously flat surface such that the wave's crests reach 10 mm into the flow. Because of the waviness of the sidewall, locally adverse pressure gradient and favorable pressure gradient flow conditions occur in the channel.

To improve the knowledge of the local variations of the streamline segment statistics and therefore to better correlate the results with the instantaneous flow state, the tomographic PIV setup consisting of four scientific complementary-symmetry metal-oxide semiconductor cameras providing a resolution of $2560 \times 2160\,\mathrm{px}^2$ at 16 bits per pixel and a dual cavity laser providing 200 mj per pulse was modified compared to previous studies [19], in which four narrow cuboid volumes along the wave were illuminated by a beam aligned in the spanwise direction and recorded separately without acquiring data from the surroundings. The modified setup provides an approximately 8-mm-thick light sheet which is arranged perpendicular to the wavy channel surface allowing for a more detailed analysis of the streamline segment statistics by capturing a wider range of wall-normal distances and a larger section of the wave. The field of view was set to capture the surroundings of the wave, where effects of the decelerating flow, i.e., separation onset due to the adverse pressure gradients, were expected. The field of view (FOV) is depicted in Fig. 3.

The evaluation process itself consisted of the well-established simultaneous multiplicative algebraic reconstruction technique volumetric intensity reconstruction [23], a direct multigrid

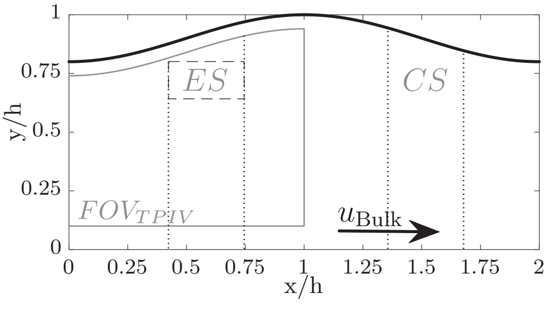

FIG. 3. Field of view (FOV) of the tomographic PIV setup. (ES) defines the FOV in Ref. [19].

correlation step [24], an motion tracking enhancement volume refinement step [25], and finally another direct multigrid correlation step. The final intensity reconstruction consisted of $2497 \times 2552 \times 418\,\text{vox}^3$ with each interrogation volume spanning $32^3\,\text{vox}^3$. At 50% overlap, the final velocity grid contained $156 \times 160 \times 26$ nodes. This corresponds to a volume in physical coordinates measuring approximately $45 \times 50 \times 8\,\text{mm}^3$ with an interrogation volume size of 0.62 mm and therefore a vector spacing of 0.31 mm. Because of the high smoothness requirement for gradient-based structure detection methods, the raw velocity fields were postprocessed by an fast Fourier transform filter to compensate for measurement noise. The impact of the filtering process and its validity is discussed in the previous study [19]. In total, 2500 independent image sets were recorded and evaluated.

Since the cameras cannot be placed within the channel, the viewing angles are not perpendicular to the thick light sheet. As a consequence, the wall reflection was visible in the captured images, prohibiting the reconstruction in immediate wall proximity. This results in a near-wall region of about 2 mm thick without reliable data. Hence, this region was masked in the source images.

B. Computational setup

The dimensions of the physical domain are $L_x = 8h$, $L_y = 2h$, and $L_z = 4h$ in the streamwise, wall-normal, and spanwise direction. The wavy surface of the lower wall of the channel has a wavelength of $\lambda = 2h = 100\,\text{mm}$ such that four waves are included within the streamwise direction. On the wall, a grid resolution in inner wall units of $\Delta_x^+ = 4.1$, $\Delta_y^+ = 1.0$, and $\Delta_z^+ = 8.2$ is used, with a relaxation of the y component toward the centerline of the channel. This yields a grid with $n_{\text{cells}} = 400 \times 120 \times 100 = 4.8 \times 10^6$ cells. Periodic boundary conditions are applied at stream- and spanwise boundaries. A no-slip boundary condition is used for the sidewalls. The Reynolds number is $\frac{u_{\text{Bulk}} h}{\nu} = 3200$ to match the experimental conditions.

Due to the sufficiently high resolution, the compressible unsteady Navier-Stokes equations are solved directly (DNS) on body-fitted grids. For the convective fluxes, the advection upstream splitting method (AUSM) is used and a central scheme is employed for the viscous terms. The temporal integration is performed by an explicit five-stage Runge-Kutta method at second-order accuracy. Among numerous other studies, investigations in Ref. [26] have shown the high quality of the results of this numerical method.

To obtain independent snapshots, the resulting data set encompasses 1000 samples with a temporal sampling rate of $\Delta t_{\text{Snapshot}} = 0.5h/u_{\text{Bulk}}$. An increased sampling rate results in multiple snapshots showing the same structures.

C. Streamline segment detection

The same streamline detection procedure was applied to experimental and numerical data. Streamlines were traced starting from 10 000 homogeneously distributed seed points per snapshot. A Runge-Kutta 4-5 scheme was used for the spatial integration while the step size was set to one fifth of the local cell size. Local velocities between the grid points were determined using cubic spatial interpolation. Consequently, the local coordinate along each streamline and the absolute velocity were calculated from the spatial coordinates and local velocities of all contributing vertices resulting in two simple vectors. Local extrema were identified as such vertices which have neighbors with purely greater or lower absolute velocities. The streamline coordinates of such vertices were refined by fitting parabolas onto their own and their neighbors' velocities and determining the analytical location of the extrema. All other vertices were discarded. A streamline segment is constituted by two neighboring extrema. Its arclength l is the difference in the streamwise coordinates of the constituting extrema, while its inner velocity difference Δ is the difference between the absolute velocity values.

III. RESULTS

The discussion of the results is divided into four sections. First, the experimental and numerical results are validated by the comparison to the planar particle-image results from Ref. [19] in Sec. III A. In Sec. III B, the streamline segment statistics are discussed with respect to the behavior of the attached and detached flow states to identify the flow condition which leads to the decreased sensitivity of streamline segments statistics to the background strain. To identify the mechanism leading to this behavior, the model equation for streamline segment probability distributions by Schäfer *et al.* [18] is extended for inhomogeneous flows in Sec. III C, applied to the DNS data, and the resulting findings are presented in Sec. III D.

A. Comparison of experimental and DNS data and validation

Before any further analyses, the results from the experimental and numerical data are compared to mutually show their quality. The data set obtained from planar PIV measurements in the previous study [19] has already been demonstrated to match the findings of Zilker and Hanratty [20] and is therefore used as reference. For this comparison, first- and second-order statistics of both data sets were averaged in the z direction since each plane should converge toward the same statistical properties due to the large span of the channel. The velocity and fluctuation profiles at several streamwise locations within one wavelength are shown in Fig. 4. Note that no tomographic PIV data are available at $x/h = 1.2$ and 1.6 due to the limited field of view shown in Fig. 3.

The mean streamwise velocities compare well for all data sets. The DNS results have a slightly flatter profile toward the centerline of the channel. In the crest region $x/h = 0$, the mean streamwise velocity distribution of the experimental data shows a plateau-like shape at $y/h \approx 0.75$. In the DNS data, this shape is less pronounced. The wall-normal component in the planar PIV data matches the DNS data in shape and in magnitude while the velocities measured by tomographic PIV exhibit an offset. This is due to a slight misalignment of the calibration target during the calibration procedure, resulting in a minimal orientational mismatch of the coordinate systems between the tomographic PIV measurements, planar PIV measurements, and DNS data. Generally, the shape of the velocity distribution matches the reference data. The magnitude of the wall-normal velocity and the offset lie within the generally accepted uncertainty of tomographic PIV of approximately half a voxel.

The streamwise velocity fluctuations of both experimental data sets match very well, while they slightly exceed the DNS data in magnitude. This is particularly visible in the fluctuation peak associated with the buffer layer. A good match between all three data sets is obtained in the wall-normal velocity fluctuation. The experimental data sets present a faster decay of the fluctuation magnitude toward the channel's center than what is found in the DNS data.

Overall, both data sets exhibit a satisfactory agreement concerning distribution and magnitude of the observed statistics, which match in terms of velocity and fluctuation distribution trends and detected features. The somewhat elevated level of velocity fluctuations found in the crest region, i.e., in the region $x/h \approx 0$, in both experimental data sets suggests a slight difference in the Reynolds number between the experimental facility and the DNS data.

B. Attached and detached flow state

While it could be shown that the mean strain has a significant impact on the streamline segment statistics and their asymmetry, the expansion slope and trough regions showed deviating behavior when large backflow events occurred, i.e., the asymmetry of the joint PDF did not scale with the background strain due to the mean local acceleration $\overline{a_{sl}} = [(\overline{\vec{v}} \cdot \nabla)\overline{\vec{v}}] \cdot \overline{\vec{t}}_v$, where $\overline{\vec{t}}_v$ is the unit vector tangential to the mean flow. While the flow is highly three-dimensional and intermittent, such backflow events are referred to as separation and otherwise is interpreted as an attached flow state. Instead, values indicating almost symmetrical distributions or even somewhat longer accelerating segments usually found in homogeneous flows were detected [19]. Since this behavior seems to be

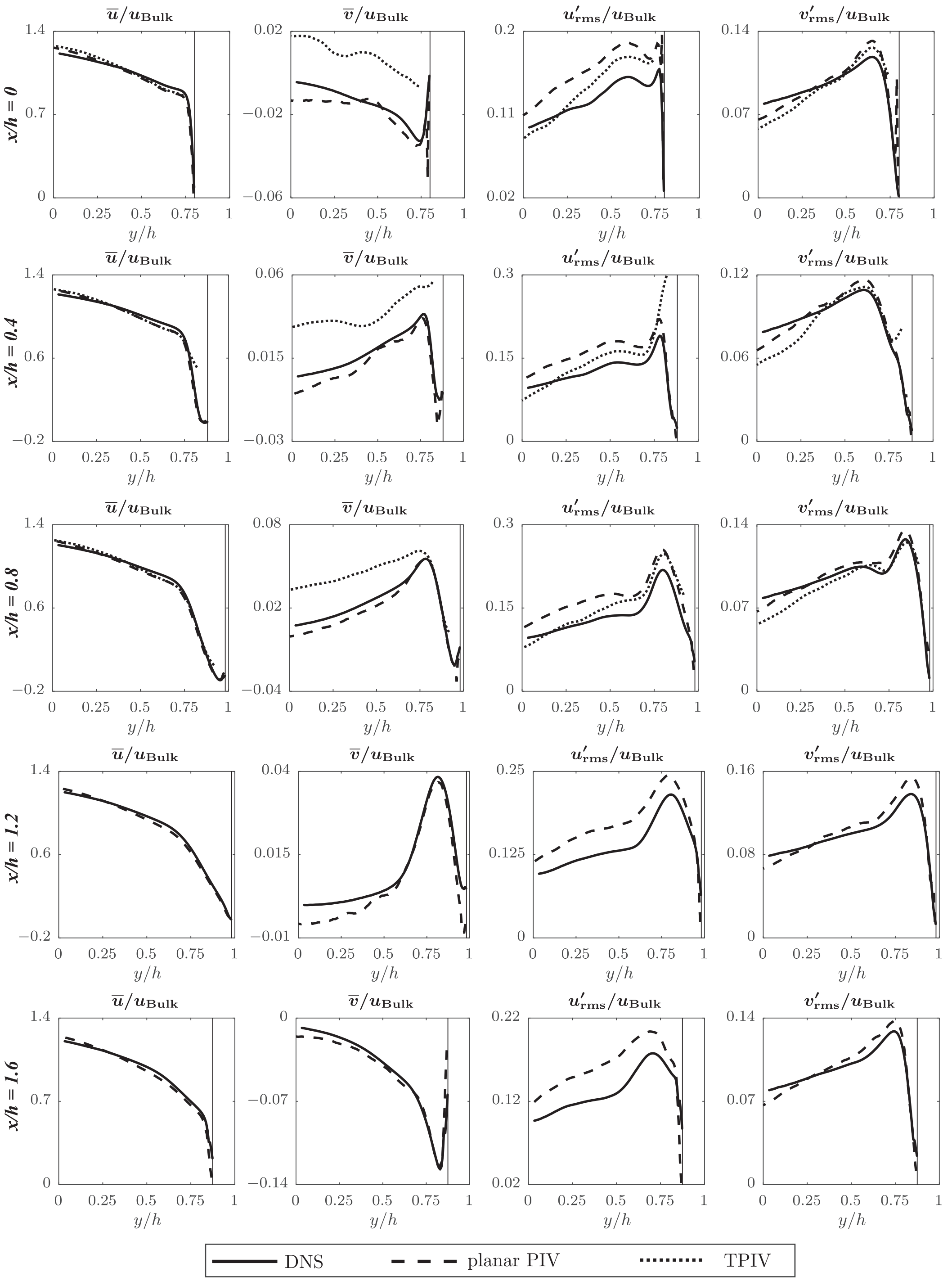

FIG. 4. Profiles of first- and second-order statistics in multiple streamwise locations. The wall position is indicated by the vertical solid line.

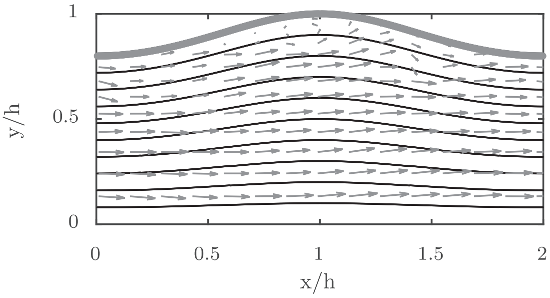

FIG. 5. Artificially generated reference flow for a fully attached flow field.

confined to the volumes with reversed flow events, a closer look at these events is required. Due to the highly unsteady flow behavior, the flow does not present a continuous detached flow region. Instead, instances of attached flow following the contour of the wave can be observed in this flow regime as well as flow detachment with the occurrence of large eruption events as noted, e.g., by Cherukat [21].

Because of the highly fluctuating nature of this flow configuration, individual snapshots do not necessarily exhibit a smooth and clearly distinguishable separation bubble. To identify samples in which separation occurs, a hypothetical flow configuration with purely sinusoidal streamlines was used as reference. The deflection of the streamlines was chosen such that it matches the wall contour and decreases linearly to zero toward the channel's centerline. The resulting streamline configuration and an instantaneous velocity field are shown in Fig. 5. The normalized scalar product between the reference streamline tangential vector $\vec{t}_{\text{ref}}$ and the tangential vector of the local velocity $\vec{t}_v$ was determined. Its volumetric average within the domain Ω in each snapshot was used to distinguish between attached and detached flow states, where high values point to the respective snapshot exhibiting an attached flow state, while low values are used to detect strong separation events. The domain Ω encompasses the full streamwise extent of the experimental FOV. It ranges from $y = 0.5$ to the wall in the wall-normal direction since the effect of the wavy sidewall becomes negligible toward the channel's center.

To determine the effect of a large detached flow region, only the 250 snapshots exhibiting the lowest values in the previously described selection criterion, i.e., 10% of all recordings, were compared to the 250 samples presenting very high numbers. In Fig. 6(a), the selection criterion for all experimentally recorded snapshots is illustrated. Additionally, the mean flow field of these two subsets are visualized by streamlines in Figs. 6(b) and 6(c), confirming that the chosen criterion is suitable to distinguish between attached and detached samples.

The same procedure was applied to the numerical data. However, due to the massively larger domain when compared to the experiment and the highly three-dimensional structure of the backflow events, a single snapshot can exhibit clearly attached and detached regions at the same time. Therefore, the domain was divided into subvolumes with a length of a single wavelength and a spanwise extent of $0.25h$. The resulting subvolumes were then considered individually and treated as independent snapshots.

The resulting selections of snapshots can be analyzed separately to determine if the deviating behavior with respect to the statistical asymmetry found in the expansion slope and trough regions is caused by the highly unsteady detachment events as described, for example, by Cherukat [21]. To further investigate the statistical asymmetry, the local ratio between mean segment lengths of accelerating and decelerating segments was determined within the streamwise range of the slope (ES) region in Fig. 3, where the deviation was first observed in Ref. [19]. Since a larger FOV is available in the current experimental data set, the extent in the wall-normal direction of the analyzed region was increased to fit the FOV. Additionally, the contraction slope region (CS) behavior found in the numerical data is considered for comparison.

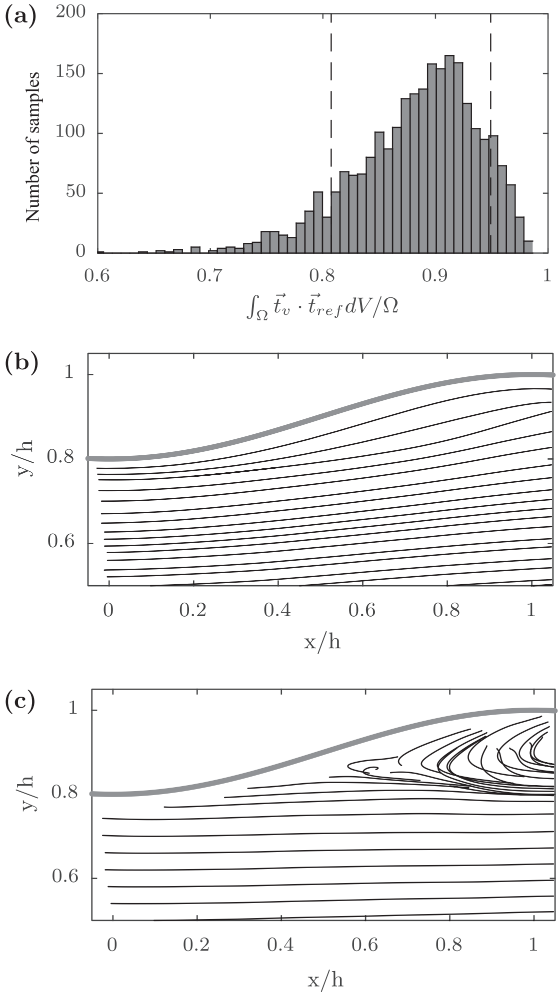

FIG. 6. Selection criterion and attached and detached flow in the TPIV data (a) Selection criterion, (b) Mean attached flow field, (c) Mean detached flow field.

Figure 7 shows the mean local acceleration $\overline{a_{sl}}$ as an indication of the local normalized background strain in the streamwise direction and the resulting statistical asymmetry based on all snapshots from the experimental data set, the samples presenting clearly attached flow, and the clearly detached samples. Overall, the mean acceleration caused by the background strain is relatively homogenously distributed at moderate negative values in large portions of the considered region. Close to the wall, a layer of much stronger deceleration with a clearly visible peak deceleration at $y/h \approx 0.8$ which decays toward the wall is observed. The subset of samples in which the flow remains attached to the sidewall is generally comparable in its shape to the distribution obtained from all snapshots. Toward the channel center $y/h = 0$, the moderate deceleration appears almost constant at roughly the same level as the overall average. From $y/h > 0.4$ on, the attached flow undergoes a stronger deceleration. The shape of the distribution remains comparable to the overall average with the deceleration peak moving closer toward the wall. In contrast to this, the subset in which the flow detaches presents a magnitude decreasing background strain reaching values of roughly zero at $y/h \approx 0.6$. Beyond this point, the detached region causes the flow to significantly decelerate, reaching its strongest deceleration at $y/h \approx 0.75$. This deceleration is far

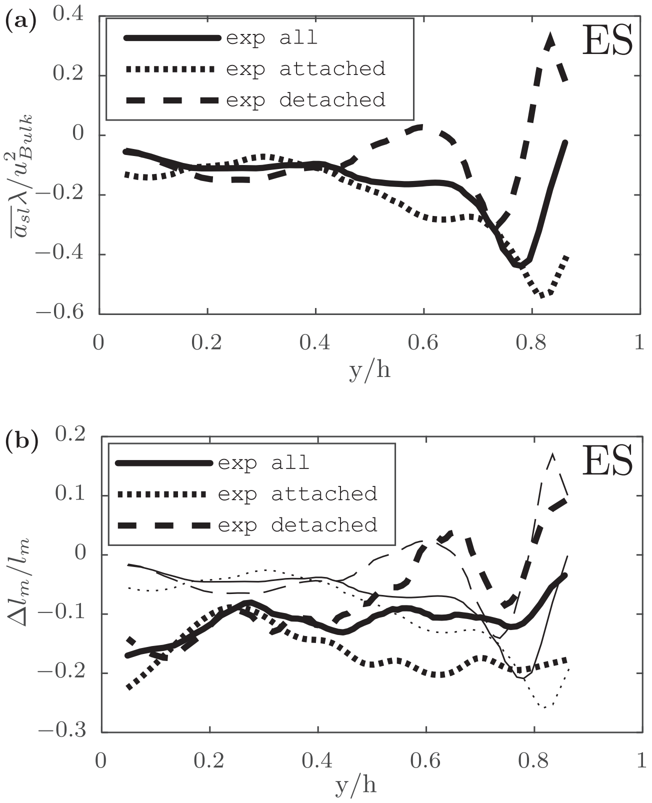

FIG. 7. Strain and statistical asymmetry in the expansion slope region (ES) based on the TPIV data (a) Normalized mean streamwise strain, (b) Ratio between the mean segment length of positive and negative segments (thick) and empirical prediction (fine).

weaker than the peaks found in either the complete sample set or particularly the attached flow case. From this point on, the background strain increases, even forming a local maximum with a value significantly larger than zero near the wall, which corresponds to the reversed flow in this layer.

The statistical asymmetries quantified by $(l_m^+ - l_m^-)/l_m$ for all samples and both subsets are also shown in Fig. 7(b). Additionally, the empirical prediction for the asymmetry from Ref. [19] is shown. It can be expressed as a linear relation between the mean acceleration and the statistical asymmetry

$$(l_m^+ - l_m^-)/l_m \approx 0.5\frac{\overline{a_{sl}}\lambda}{u^2_{\text{Bulk}}} + 0.01.$$

Toward the centerline of the channel at $y/h < 0.2$, a steep decline of the segment length ratio can be observed. This is likely an artifact of the boundary of the measurement volume, which causes the streamline detection to omit segments extending beyond the measurement volume. Decelerating segment detection is more likely since those segments tend to point toward the wave's trough and therefore reach further into the measurement volume. Additionally, this distinct behavior is confined to the near boundary region where the DNS data shown in Fig. 8 do not show a comparable trend. Beyond $y/h = 0.2$, the streamline segment asymmetry in Fig. 7(b) reflects the trends that are observed in the local mean acceleration in Fig. 7(a). The detached subset exhibits the smallest absolute asymmetries while the attached subset shows a much larger asymmetry. The statistics obtained from the detached subset in Fig. 7(b) correlate

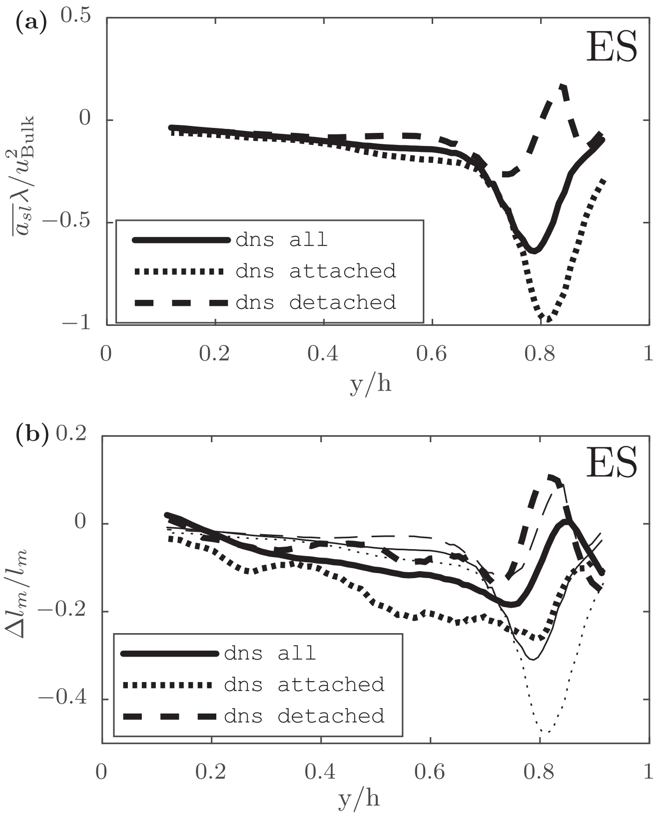

FIG. 8. Strain and statistical asymmetry in the expansion slope region (ES) based on the DNS data (a) Normalized mean streamwise strain, (b) Ratio between the mean segment length of positive and negative segments (thick) and empirical prediction (fine).

closely with the respective background strain in Fig. 7(a). That is, the local extrema occur at comparable positions. The attached subset and the overall statistics possess roughly constant asymmetry values in the range of $0.4 < y/h < 0.8$. Neither set shows a clear peak at $y/h \approx 0.8$ comparable to the one found in the mean acceleration in Fig. 7(a). This is particularly apparent when the empirical relation between the mean acceleration and the streamline segment asymmetry depicted by the fine lines is considered as reference. While it underestimates the impact of the background strain in the range $0.4 < y/h < 0.7$, the general shape of the asymmetry is predicted well. In the region $y/h > 0.7$, only the detached subset curve resembles the prediction based on this relation. The attached flow state and the overall statistics do not exhibit the large asymmetry peak near the wall, which is predicted based on the background strain. Consequently, this suggests that the deviation from the previously observed relation is not determined by the separation. Rather, the large compressive strain coinciding with near-wall shear of the attached flow state appears to cause segments to break. Additionally, the data obtained from the current setup suggests that the coefficient for the linear relation between the two quantities is higher than estimated in Ref. [19] for moderate accelerations. A possible reason for the underestimation in the previous study is the smaller measurement volume, which suppresses long segments, which in turn are responsible for large asymmetries.

Analogously, the corresponding data obtained from the DNS data are shown in Fig. 8. The essential findings from the experimental data are confirmed. The detached subset of samples exhibits a strong correlation between the mean acceleration in Fig. 8(a) and the streamline statistic

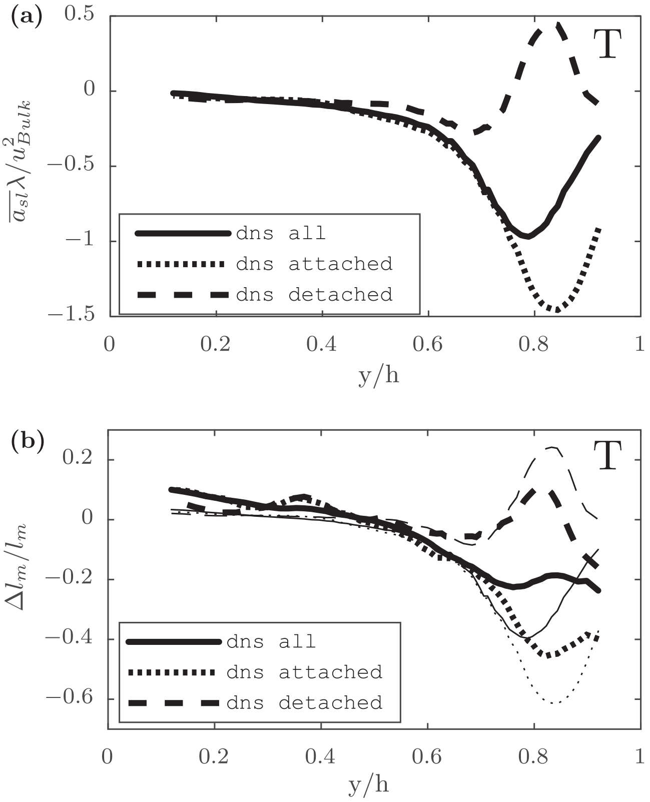

FIG. 9. Strain and statistical asymmetry in the trough region (T) based on the DNS data (a) Normalized mean streamwise strain, (b) Ratio between the mean segment length of positive and negative segments (thick) and empirical prediction (fine).

asymmetry in Fig. 8(b). In line with the experimental data, the attached subset in Fig. 8(b) does not form the pronounced peak which the mean acceleration in Fig. 8(a) suggests. In the region between $0.4 < y/h < 0.7$, the segment length ratios of all subsets show the same trend as the mean acceleration. That is, the barely decelerated detached subset exhibits a smaller streamline length ratio than the subset of the attached samples. The prediction in the previous study [19] underpredicts this effect. This is consistent with the findings from the current experimental data. A notable difference between the experimental and numerical data sets is the trend of the segment length ratio toward the center of the channel. All three sample sets of the DNS data in Fig. 8(b) tend toward zero or even slightly positive values. This is in good agreement with the prediction by Wang for homogeneous shear flows [15] since the influence of the wavy wall diminishes toward the channel's centerline. Consequently, the deviating behavior observed in the experimental data set in this regard appears to be an effect caused by the finite FOV.

In the trough region, the subsets for attached and detached flow conditions correlate well with the mean acceleration as shown in Fig. 9. However, the magnitudes of the observed asymmetries are well below their respective predictions. This is in good agreement with observations in Ref. [19], where the linear relation was not valid in the trough region. As a result, the overall asymmetry does not reflect the peak in the local mean acceleration. This is expected since the mean deceleration magnitude is comparable to the magnitude found in the attached subset of the expansion slope region, in which the correlation to the asymmetry neither matched.

The mean acceleration in the contraction slope region and the corresponding segment length ratios are shown in Fig. 10. In contrast to the more complex flow structure in the separation region,

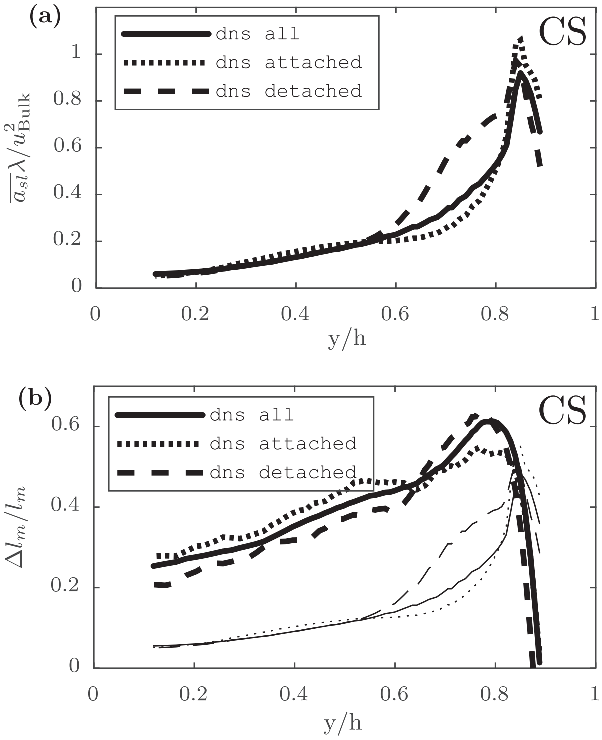

FIG. 10. Strain and statistical asymmetry in the contraction slope region (CS) based on the DNS data (a) Normalized mean streamwise strain, (b) Ratio between the mean segment length of positive and negative segments (thick) and empirical prediction (fine).

the mean acceleration in this region exhibits only positive values, due to the contracting sidewall contour, which reach a distinct peak close to the wall and decrease toward the channel center where the sidewall effect diminishes. The mean acceleration profiles show a difference; i.e., in the detached case the near-wall acceleration region is wider with a smaller near wall peak than what is determined in the attached sample subset. While the segment length ratios in Fig. 10(b) follow the overall trend with the largest statistical asymmetries near the wall, the location of the near-wall peak is somewhat shifted off the wall compared to the location in the mean acceleration. Like in the expansion slope area, the effect exceeds the predictions of the previous study.

When the streamline segment statistics are evaluated locally in a number of small subvolumes homogeneously distributed across the entire domain by considering only those segments passing each volume, a quasilinear relation between $\Delta l_m/l_m$ and $\overline{a_{sl}}$ can be observed, as shown in Fig. 11. Each data point corresponds to the streamline segment distribution in a specific location. Because of the asymmetric flow within each wave, locations experiencing deceleration are significantly more abundant than accelerating locations, which are confined to a small region near the contraction slope. As previously observed in the individual regions, the linear relation is limited to moderate mean accelerations and corresponding background strains. The streamline segment statistics can reach larger degrees of asymmetry during acceleration, i.e., expansive strain, than during deceleration, i.e., compressive strain, before showing asymptotic behavior. Additionally, some states shown in the figure do not adhere to the linear relation and resemble hysteretic behavior, indicating that the structures convected through this flow field cannot adapt to their new surroundings immediately and do not reach an equilibrium state suiting the local conditions. Even though a large portion of the flow is decelerated, the overall mean acceleration within this periodic domain is zero. Because of the

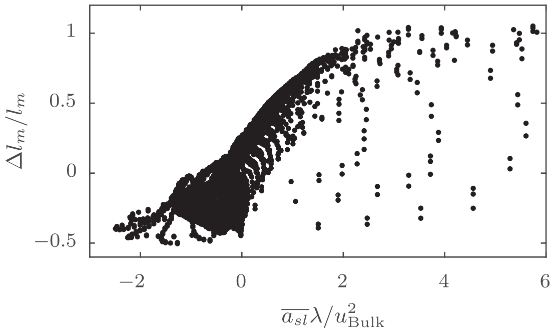

FIG. 11. Overall relation between local normalized acceleration and streamline segment length ratio based on the DNS data.

larger linear range of positive asymmetries, the overall asymmetry will remain positive and resemble the streamline segment statistics obtained from isotropic turbulence, which has been shown by Hennig *et al.* [27]. Note that higher $\overline{a_{sl}}$ values are observed in this case when compared to the data from the wall-normal subvolume shown in Fig. 3. The high values originate from small, highly localized spots close to the wall. Because of the evaluation per layer and the streamwise extent of the wall-normal subvolume, these highly local data points only contribute to the final value of the profile like more moderate neighboring values do, which occur more often, as seen in Fig. 11.

The separate discussion of the attached and detached flow states evidences the immediate effect of local strain acting upon the streamline segments during local acceleration and deceleration. It is even more apparent than found in Ref. [19]. For each state, a close correlation between the streamline segment asymmetry and the mean acceleration can be observed. Contrary to former expectations, the deviation from their approximately linear relation appears to be generated by the strong compressive background strain which occurs during the deceleration in the attached flow state. When passing the expansion slope region, streamline segments cannot adapt instantly to the surrounding conditions. Only after having undergone deceleration for a while, an apparent correlation between the background strain and the streamline segment asymmetry is recovered in the trough region, albeit falling short of the prediction.

While the state-based consideration of the collected data gives insight into the origin of the occurring effects, any sort of prediction cannot rely on the knowledge of a number of exact snapshots and their respective attachment or detachment state since fully resolved and statistically categorized data would render further predictions unnecessary. A model that explains the observed effects is definitely more interesting. Therefore, the streamline segment propagation equation proposed by Schäfer *et al.* [18] will be considered and adapted to account for this inhomogeneous flow in the following section.

C. Streamline segment statistics propagation equation under inhomogeneous conditions

To identify the mechanisms causing the local phenomena within the streamline segment statistics, the propagation equation proposed by Schäfer *et al.* [16,18] building on the propagation equation for dissipation elements by Wang and Peters [28] is applied to the local joint probability distribution (jPDF) of streamline segment length and inner velocity difference obtained from the DNS results. In the following, two kinds of categorization will be used when discussing streamline segments. A type of streamline segment will refer to either accelerating $\Delta > 0$ and decelerating segments $\Delta < 0$. A class encompasses all segments with a specific combination of length l and inner velocity difference Δ. The original form of the propagation equation is expressed per segment class. It is based on a Poisson process and has previously been applied to forced and decaying as well as shear turbulence. Since it was derived for homogeneous turbulence, the probability distribution is considered homogeneous in space such that all detected segments are considered regardless of their position in space. Therefore, the jPDF is also independent of any position $\vec{x}$:

$$\begin{aligned}&\frac{\partial}{\partial t}P(l,\Delta,t)+\frac{\partial}{\partial l}[a_{1,l}P(l,\Delta,t)]+\frac{\partial}{\partial \Delta}[a_{1,\Delta}P(l,\Delta,t)]\\&=\lambda_c\left(\underbrace{2\int_0^\infty\int_l^\infty\delta\left(\psi k\left(\frac{l}{y}\right)-\Delta\right)P(y,\psi,t)dyd\psi}_{\text{GC}}-\underbrace{lP(l,\Delta,t)}_{\text{RC}}\right)\\&\quad+2\mu_a\left(\underbrace{\int_0^\Delta\int_0^l\frac{y}{l}P(l-y,\Delta-\psi,t)P(y,\psi,t)dyd\psi}_{\text{GR}}-\underbrace{P(l,\Delta,t)}_{\text{RR}}\right).\end{aligned}$$

This propagation equation describes two types of processes which streamline segments undergo. The first type is a slow drift in length l as well as in inner velocity difference Δ, which continuously occurs due to stretching and diffusion. These effects are represented by their respective drift terms $a_{1,l}$ and $a_{1,\Delta}$, which can be expressed by

$$\begin{aligned}a_{1,l}&=-\frac{c_{l,\nu}}{l}\{1-c_s[1-\exp(-2l)]\}+C_\Delta\Delta,\\a_{1,\Delta}&=-c_{\Delta,\nu}\frac{\Delta}{l^2}\exp(-3l)+\text{sgn}(\Delta)K+\frac{\Delta}{\tau^{+,-}}.\end{aligned}$$

The lengthwise drift term $a_{1,l}$ consists of two parts. The first part describes the diffusive change of segment length. Short segments in particular decay on average, which is expressed by $-c_{l,\nu}/l$. This can only occur when the two defining local extrema of the streamline segment move toward each other such that the neighboring segments grow in length. This is expressed through the following expression, in which the value of c_s is chosen such that the overall change of length of all segments is zero. The second part of the lengthwise drift represents the growth or decay of streamline segments due to their inner kinematics. Accelerating segments possess a leading extremum with a higher velocity than the trailing one, which causes it to grow over time. The opposite is true for decelerating segments. The parameter C_Δ reflects the impact by the instantaneous streamwise pressure distribution, counteracting the segment stretching and compression kinematics. It assumes values between zero and one.

The velocity drift term $a_{1,\Delta}$ consists of three contributions. In analogy to the lengthwise drift, the contribution lead by $c_{\Delta,\nu}$ represents the diffusive decay of local velocity extrema, leading to a decrease in the segments' inner velocity difference Δ. The source term $\text{sgn}(\Delta)K$ is required to maintain statistical equilibrium in homogeneous turbulence [18]. The third term describes the inner velocity evolution due to the segment kinematics. Note that the associated timescales assume different values for accelerating (τ^+) and decelerating (τ^-) segments.

The second type is a breakup or cutting process, which occurs when the zero velocity gradient surface moves onto a previously monotonous streamline segment, instantaneously cutting it into two pieces. A reversal of this process causes a small segment to disappear by effectively reattaching two neighboring segments. While each of these instantaneously occurring effects represents a single process, they are represented by two terms in the equation. A particular class of streamline segments can be generated by the cutting (GC) or reattachment (GR) processes. At the same time, these processes also remove segments of that class from the distribution, which is expressed by RC and RR. The redistribution within the jPDF due to the instantaneous processes depends only on the jPDF itself and the occurrence rates λ_c and μ_a.

The statistical consideration of the streamline segments from all snapshots leads to an effectively time-averaged representation, in which the temporal derivative is zero. Unlike in Ref. [18], the probability distribution is now a function of the position in the domain $\vec{x}$ due to the inhomogeneity

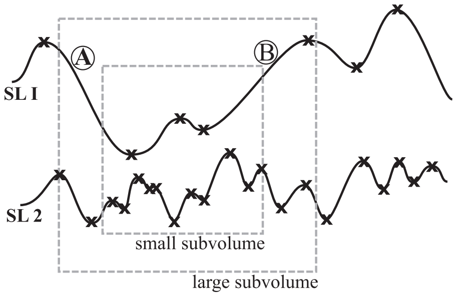

FIG. 12. Schematic of streamline segment selection based on subvolumes.

in the current study and therefore it requires the addition of a convective term $\vec{v}\cdot\nabla P(\vec{x},l,\Delta)$ to represent the local propagation of the segments within the flow field

$$\begin{aligned}\underbrace{\frac{\partial}{\partial t}P(\vec{x},l,\Delta)}_{=0} + \vec{v}\cdot\nabla P(\vec{x},l,\Delta) + \frac{\partial}{\partial l}[a_{1,l}P(\vec{x},l,\Delta)] + \frac{\partial}{\partial \Delta}[a_{1,\Delta}P(\vec{x},l,\Delta)] \\ = \lambda_c\left(2\int_0^\infty\int_l^\infty \delta\left(\psi k\left(\frac{l}{y}\right)-\Delta\right)P(\vec{x},y,\psi)dy\,d\psi - lP(\vec{x},l,\Delta)\right) \\ + 2\mu_a\left(\int_0^\Delta\int_0^l \frac{y}{l}P(\vec{x},l-y,\Delta-\psi)P(\vec{x},y,\psi)dy\,d\psi - P(\vec{x},l,\Delta)\right).\end{aligned}$$

Note that the newly introduced local dependence of the jPDF is not straightforward since the segments have a spatial extent such that they are not unambiguously associated with a single position in space. The simplest way to deal with local statistics is a subdivision of the flow domain into smaller subvolumes, in which the local streamline segment statistics can be obtained as if they were homogeneous. However, to achieve a high degree of localization the subvolumes must be small. Since streamline segment length distributions can span the entire range of turbulent length scales, the evaluation of very small subvolumes will omit large segments, introducing a bias toward small segments. Large subvolumes can capture such segments at the cost of a clearly local probability distribution since the result will be a volumetric average distribution of the entire subvolume. Additionally, any subvolume-based localization method will suffer from boundary effects, introducing an additional bias since large segments can only be detected if they entirely fall into the subvolume. Therefore, segments with lengths close to the subvolume length will only be detected if they are located in the center of the volume while small segments can be detected anywhere in a subvolume if they do not cross the subvolume's boundary.

A sketch of the subvolume approach is shown in Fig. 12 with two subvolumes. For two exemplary streamlines, the velocity distribution is shown and the local extrema defining the streamline segments are marked. Streamline 1 is comprised of mostly long segments. Two relatively long segments are labeled A and B. When the small subvolume is considered, it is obvious that neither segment A nor segment B can be captured, leaving only the two segments in between as local segments, which cover only about half of the subvolume length. For the larger subvolume, segment B falls entirely into the subvolume, while the segment A requires the size to be increased even further to be locally captured. In contrast, streamline 2 consists of rather short segments. Therefore, the part of the streamline that is considered local is much less sensitive to the subvolume size. For both subvolume sizes, the number of streamline segments is much larger than what is found for streamline 1. This clearly illustrates how a locality definition based on a subvolume will introduce bias toward small segments.

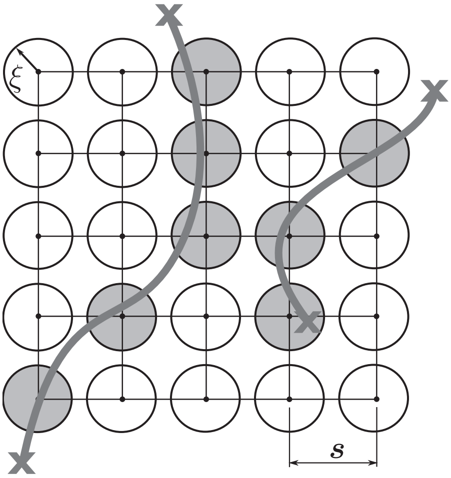

FIG. 13. Association of streamline segments with grid points.

To unify these seemingly contradicting requirements, a different concept of streamline segment locality is introduced in this study. Instead of subdividing the spatial domain, locality is determined on a per-segment basis. Each segment is associated with all points in the flow domain it passes. Therefore, all segments that have passed a certain point in space constitute the set from which the local probability distribution can be obtained. The main benefit of this approach is that it does not introduce any spatial limits that can lead to the omission or bias toward a certain class of segment. Nonetheless, it provides an exact localization scheme which can be evaluated at any point within the flow domain.

Since fully converged statistics are required for any further analysis, a single streamline segment per snapshot and point of interest is not sufficient. Therefore, the localization approach was adapted such that all streamline segments passing the point of interest within close proximity of ξ contribute to its probability distribution. A schematic of this approach is shown in Fig. 13. A grid of points where local probability distributions are evaluated are passed by two exemplary streamline segments. All points in close proximity to the streamline segment are highlighted as the segment will contribute to the probability distributions of those points.

In his original study [15], Wang elaborates on the equivalence of volume weighting of streamtube segments and the averaging over all streamline segments determined by tracing streamlines from a homogeneously spaced grid. This argument was later used to derive the model equation for the length distribution of dissipation elements [28] and streamline segments [16] and the equation for the joint probability distribution of streamline segments [18] determined by a balance of grid points occupied by a certain class of structure. However, due to the chosen locality definition in this study, each streamline segment can contribute to the statistics of more than one cell of the statistics grid, invalidating the conservation of grid points and direct volume weighting in the event of cutting or reattachment.

To account for this, the propagation equation's terms representing the segment generation by cutting and reattachment processes (GC and GR) have to be adapted. While the terms responsible for the removal of streamline segments RC and RR refer to streamline segments already included in the local jPDF, the generation terms GC and GR are subject to the localization scheme such that only one fragment of a newly cut segment will be registered locally. Analogously, a newly merged long segment will be registered anywhere, where one of its original parts was registered as well.

Except for the δ function introduced by Schäfer *et al.* [18] to distinguish between classes of streamline segments which differ only in their inner velocity difference, the fundamental derivation of this term was done by Wang and Peters [28] by counting all grid points which are transferred to

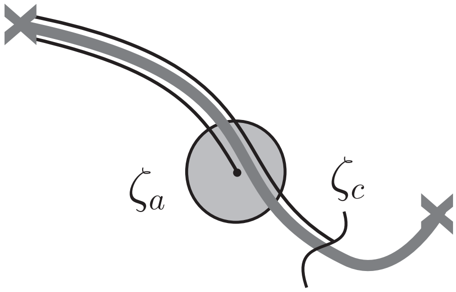

FIG. 14. Detection and cutting location for a single streamline segment.

the segment class of length l

$$\frac{\partial}{\partial t}[n_l P(l)]_{\mathrm{GC}} = \lambda_c \int_l^\infty P_{y\to l}\, n_y\, yP(y)dy.$$

The term $P_{y\to l}$ reflects the average fraction of grid points that is transferred to class l, when a segment of class y is cut, the quantity n_y represents the number of grid points in class y, and $yP(y)$ counts the number of segments of class y being cut. In the original publication, it is assumed that all grid points from segments being cut will be redistributed to other classes and that the occurrence rate of each resulting class is the same such that $P_{y\to l}$ must be proportional to the resulting length l. Therefore, $P_{y\to l}$ is determined to be of the form

$$P_{y\to l} = Al.$$

Its integral between zero and y must be one, which allows the coefficient A to be determined.

In the current study, this is not the case. Rather, the number of grid points, which will remain part of the local streamline segment ensemble, depends on the relative position where the cutting event occurs ($\widetilde{\zeta_c} = \zeta_c/l$) and the relative position where the original segment passes the cell with which it is associated ($\widetilde{\zeta_a} = \zeta_a/l$). Analogously to the original derivation, the probability density of cuts along the segment is assumed to be uniform. The probability density of the associated cells' relative position within the segment must be uniform as well, since their spatial distribution is homogeneous. Effectively, this results in $P(\widetilde{\zeta_c}, \widetilde{\zeta_a}) = 1$ for all $\widetilde{\zeta_c}$ and $\widetilde{\zeta_a}$. A schematic of these two positions is shown in Fig. 14.

To calculate the average fraction of grid points which remain part of the local ensemble, two cases can be considered. If the cell is located between the beginning of the segment and the cut, the fragment of the segment associated with the cell has a normalized length of $\widetilde{\zeta_c}$. Since the number of grid points in a segment only depend on the segment length, the fraction of grid points which remain local also assumes the value of $\widetilde{\zeta_c}$. This is represented by the first term of the equation below. If the cell position lies beyond the location of the cutting event, only the fragment of length $1 - \widetilde{\zeta_c}$ remains local, which is expressed by the second term. The integration over all possible cut and cell locations yields

$$\int_0^1 \left(\int_0^{\widetilde{\zeta_c}} \widetilde{\zeta_c}\, \underbrace{P(\widetilde{\zeta_c}, \widetilde{\zeta_a})}_{=1} d\widetilde{\zeta_a} + \int_{\widetilde{\zeta_c}}^1 (1 - \widetilde{\zeta_c})\, \underbrace{P(\widetilde{\zeta_c}, \widetilde{\zeta_a})}_{=1} d\widetilde{\zeta_a} \right) d\widetilde{\zeta_c} = \frac{2}{3}.$$

Not only does this illustrate that one fragment of a previously cut segment becomes nonlocal but it also indicates that the locality definition causes long fragments to be more likely to remain part of the local ensemble than small ones. To account for this, $P_{y\to l}$ is modified such that it is not only proportional to the length of the receiving segment class but also scaled by the probability that the fragment will be part of the remaining segment ensemble. Because of the homogeneous distribution of statistic cells, this probability is simply l/y. The resulting and adapted distribution function

$P^*_{y\to l}$ is

$$P^*_{y\to l} = A^*\frac{l^2}{y},$$

where A^* is the coefficient possessing a new value. As shown, only a fraction of the grid points remains local when a segment is cut. Therefore, the integral must yield

$$\int_0^y P^*_{y\to l}dl = \frac{2}{3}.$$

The adapted term GC* will therefore take the following form:

$$\frac{\partial}{\partial t}P(l,\Delta)_{\mathrm{GC}^*} = 2\lambda_c\int_0^\infty\int_l^\infty \delta\left(\psi k\left(\frac{l}{y}\right) - \Delta\right)\frac{l}{y}P(y,\psi)dyd\psi.$$

The adaptation of GR is somewhat more straightforward. The original derivation integrates over the probability of all segment classes with smaller parameters for l and Δ than the target class multiplied by the occurrence probability of a neighboring segment with the length and velocity difference suitable to form a segment of the target class. Each merging segment of length y will contribute n_y grid points to the target class:

$$\frac{\partial}{\partial t}[n_l P(l,\Delta)]_{\mathrm{GR}} = 2\mu_a\int_0^\Delta\int_0^l P(l-y,\Delta-\psi)n_y P(y,\psi)dyd\psi.$$

When divided by n_l, the resulting expression will include the factor n_y/n_l, which is equivalent to the length ratio of contributing and target segment length. However, under the current locality definition, only one fragment of the newly created segment is part of the local streamline segment ensemble prior to the reattachment event. This means that the missing segment grid points will be added to the already considered segments' grid points. As a consequence, every reattachment event will contribute n_l instead of n_y grid points to the target segment class. The ratio of segment lengths must therefore vanish in the adapted expression for GR*:

$$\frac{\partial}{\partial t}P(l,\Delta)_{\mathrm{GR}^*} = 2\mu_a\int_0^\Delta\int_0^l P(l-y,\Delta-\psi)P(y,\psi)dyd\psi.$$

D. Application of the adapted propagation equation

To be able to compare the current results to previous studies, all quantities are made dimensionless by $\sigma(\vec{x}) = \langle\Delta^2|\vec{x}\rangle^{\frac{1}{2}}$, $l_m(\vec{x}) = \langle l|\vec{x}\rangle$, or a suitable combination thereof. Local dimensionless streamline segment probability distributions were calculated on a regular Cartesian grid in the range of $x/h \in [0,\ 2]$ and $y/h \in [0.5,\ 1]$. With a grid spacing s of $0.01h$, this yields 201×51 local probability distributions. For satisfying statistical convergence, the proximity parameter ξ was chosen to be $0.01h$, yielding the segment count distribution shown in Fig. 15. In each cell, the jPDF was determined spanning $l/l_m \in [0,\ 3.5]$ and $\Delta/\sigma \in [-3.5,\ 3.5]$ discretized into 20 by 40 bins.

By definition, each positive segment is followed by a negative one and vice versa such that in pure numbers, both types of segments should occur with the same probability. However, the locality definition causes each segment to be assigned to multiple cells on the statistics grid. Because of this locality definition, long segments are assigned to more cells than short segments, increasing their occurrence rate per cell. This leads to an unbalanced jPDF in which there is not necessarily the same number of positive and negative segments assigned to each cell. While this might be an accurate representation of the time each cell is occupied by positive or negative segments, this poses a problem when convective fluxes are considered since incoming and outgoing fluxes at each cell might not have the same ratio between positive and negative segments. This would require a mechanism capable of transforming accelerating segments into decelerating ones and vice versa which, by definition, is impossible because there is no segment type for which the velocity

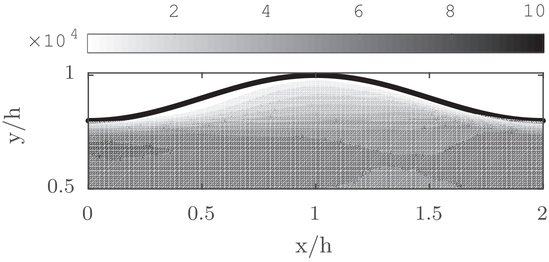

FIG. 15. Number of segments detected per cell.

difference is zero. Yet, any transformation between these two types of segments would have to pass this state. In fact, the slow drift processes merely change the length and inner velocity difference of the segments such that the probability distribution is deformed. While the fast cutting and merging processes change the number of segments contributing to the distribution, they cannot change the ratio between positive and negative segments since a merging process removes two segments and creates one larger segment of one type of segments. At the same time, the merging can only occur due to the removal of a small segment of the opposite type. Consequently, one segment of each type is removed and the ratio between the two types is not altered. The reversal of this process occurs when segments are cut.

The original number ratio between positive and negative segments is shown in Fig. 16. In regions of large statistical asymmetry, e.g., the contraction slope at $x/h \approx 1.6$, the occurrence of very long accelerating segments is increased, leading to a higher detection rate of this segment type. To avoid the need for a process capable of transforming between the two types of streamline segments, the detected local jPDFs are rebalanced such that

$$\int_0^\infty \int_0^\infty P(l, \Delta) d\Delta dl = \int_0^\infty \int_{-\infty}^0 P(l, \Delta) d\Delta dl = \frac{1}{2}.$$

Note that a similar approach is taken by Schäfer *et al.* [18]. The jPDF is iteratively approximated by the given propagation equation and renormalized after each iteration, until it reaches a steady state. In the current study, however, the local jPDFs are given and the parameters of the propagation equation are fitted. To guarantee that the propagation equation can adequately represent the local jPDF and flux, the rebalancing is required.

After balancing all jPDFs, its convective fluxes were determined. In contrast to [18], the timescales τ_{l_m} and τ_σ associated with the rate of change of the reference values l_m and σ have to be considered due to their convective change. This means that even two neighboring dimensionless jPDFs presenting the same distribution will have a nonzero flux if the reference values are not the same, since they do not represent the same segment classes in dimensional values. This change in segment classes must be reflected by some local process. Therefore, the convective flux is extended

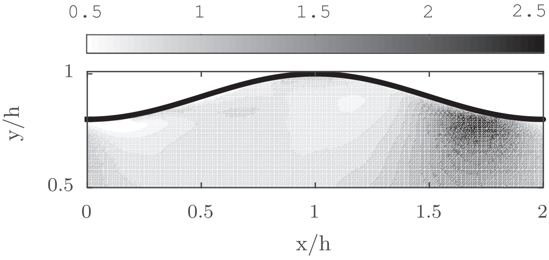

FIG. 16. Ratio between positive and negative segment numbers.

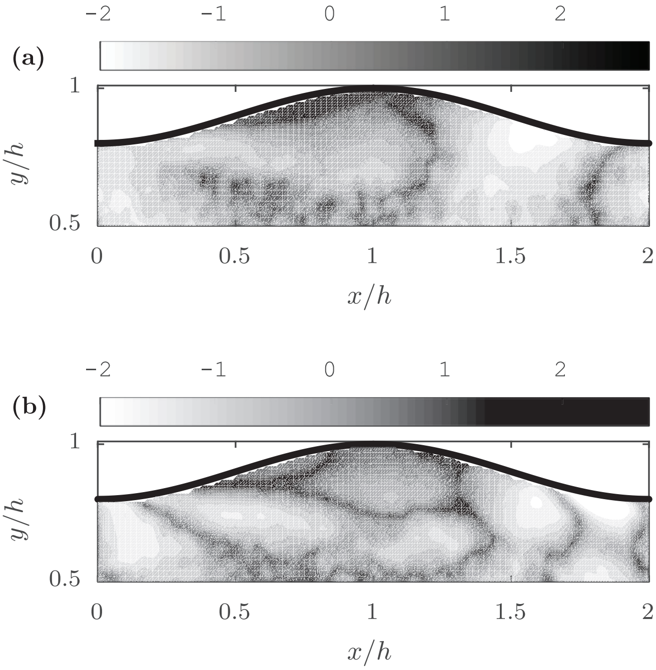

FIG. 17. Logarithm to base 10 of the magnitude of convective time scales (a) Logarithm of $\tilde{T} l_m$ (b) Logarithm of $\tilde{T}\sigma$.

by expressions to account for the convective change of the normalization references

$$\left.\frac{d\widetilde{P}}{dt}\right|_{\mathrm{conv}} = (\vec{v}\cdot\nabla)\widetilde{P} + \underbrace{\left(\frac{1}{l_m}\frac{dl_m}{dt}\right)}_{1/\tau_{l_m}}\tilde{l}\frac{\partial\widetilde{P}}{\partial\tilde{l}} + \underbrace{\left(\frac{1}{\sigma}\frac{d\sigma}{dt}\right)}_{1/\tau_{\sigma}}\tilde{\Delta}\frac{\partial\widetilde{P}}{\partial\tilde{\Delta}}.$$

To obtain τ_{l_m} and τ_σ, l_m and σ are determined locally and their spatial gradients are calculated. Since the local normalization parameters refer to the converged statistics of a large number of snapshots, their local rate of change is zero. Therefore, the required time scales are of purely convective nature, which are specific to inhomogeneous flows. They can be expressed by

$$\tau_{l_m} = \frac{l_m}{\vec{v}\cdot\nabla l_m} \text{ and } \tau_\sigma = \frac{\sigma}{\vec{v}\cdot\nabla\sigma}.$$

The $\tilde{\cdot}$ notation defines the dimensionless quantities. Note that $\frac{d\widetilde{P}}{dt}|_{\mathrm{conv}}$ is not fully dimensionless, yet. Thus, the convective rate of change is still based on dimensional time. Therefore, with nondimensional time, the final expression is

$$\left.\frac{d\widetilde{P}}{d\tau}\right|_{\mathrm{conv}} = \frac{l_m}{\sigma}\left[(\vec{v}\cdot\nabla)\widetilde{P} + \left(\frac{1}{l_m}\frac{dl_m}{dt}\right)\tilde{l}\frac{\partial\widetilde{P}}{\partial\tilde{l}} + \left(\frac{1}{\sigma}\frac{d\sigma}{dt}\right)\tilde{\Delta}\frac{\partial\widetilde{P}}{\partial\tilde{\Delta}}\right].$$

The importance of the timescales in this case can be observed when logarithmically plotting their magnitude within the flow domain as shown in Fig. 17. Only very confined regions have very large values. Most of the flow is dominated by dimensionless timescales below ten. Schäfer *et al.* [18] note timescales for the inner velocity evolution of $\tilde{\tau}^+ \approx 4.7$ and $\tilde{\tau}^- \approx 7.6$. While these timescales will be redetermined based on the inhomogeneous data, this serves as an argument that τ_{l_m} and τ_σ cannot be neglected *ad hoc*. Additionally, since the reference variables l_m and σ do not monotonously increase or decrease within the flow domain, positive and negative timescales will occur.

TABLE I. Free model parameters and values for homogeneous turbulence [18].

$\widetilde{c_{l,\nu}}$	0.5
$\widetilde{c_{\Delta,\nu}}$	1.0
$\widetilde{C_{\Delta}}$	0.1
$\widetilde{K}$	0.05
Λ_c	1.155
Λ_a	$2\Lambda_c$
$\widetilde{\tau}^{+/-}$	4.695/7.633

With the local jPDFs and fluxes available from DNS data, the model equation and parameters can be linearly fitted to the given data in each cell of the grid. More details concerning the parameter fitting procedure are provided in the Appendix. A list of the free parameters of the model function and the values reported by Schäfer *et al.* [18] for the homogeneous decaying and forced turbulence DNS are given in Table I. Note that the occurrence rates of the fast processes $\Lambda_c = \lambda_c \frac{l_m^2}{\sigma}$ and $\Lambda_a = \mu_a \frac{l_m}{\sigma}$ are given in dimensionless form. Additionally, to maintain a steady state, Schäfer *et al.* [18] set their ratio to two.

When used in the inhomogeneous wavy flow, these parameters resulted in very large residuals as they were unable to correctly approximate the fluxes, where the residual R is defined as the mean of the squared difference between the statistically detected PDF flux and the flux calculated based on the fitted parameters over all N discrete PDF bins:

$$R = \frac{1}{N}\sum_{i}^{N}\{[\widetilde{(\vec{v}\cdot\nabla)}\widetilde{P}]_{\text{stat}} - [\widetilde{(\vec{v}\cdot\nabla)}\widetilde{P}]_{\text{fit}}\}^2.$$

A fully free fit reduces the residual significantly but results in a very low magnitude and somewhat patchy parameter distribution for $\widetilde{c_{l,\nu}}$ which does not seem to be correlated to the local flow conditions. Additionally, merging events require the diffusive decay of small segments, causing their neighbors to reattach. As a consequence, with near-zero diffusion, negative segments would only asymptotically decrease in length because of their inner kinematics and cutting events without any mechanism to increase their length. Since this behavior is not observed but the periodicity of the wave is resembled in the streamline statistics, a certain degree of lengthwise diffusion is required such that decelerating segments can merge and maintain a nonzero mean length. Therefore, the parameters were also fitted with $\widetilde{c_{l,\nu}}$ fixed at 0.5 as was done by Schäfer *et al.* in Ref. [18]. The resulting residual remained low and within the range of statistical uncertainty to the fully free fit. This indicates that the larger diffusive contribution can be compensated by other mechanisms to effectively result in the same flux. This means that the parameter optimization can effectively yield a number of nearly equivalent results from a solution space. To obtain a single unique solution, at least one parameter has to be fixed. The quantity $\widetilde{c_{l,\nu}} = 0.5$ is a good candidate since it represents a viscosity-driven phenomenon which has been made dimensionless to account for the local structure sizes. Alternatively, fixing $\widetilde{c_{\Delta,\nu}}$ resulted in significantly increased residuals. The residuals for the fully free fit, the fit with a fixed $\widetilde{c_{l,\nu}} = 0.5$, the fit with a fixed $\widetilde{c_{\Delta,\nu}} = 1.0$, and the fit with the first four parameters matching the Schäfer *et al.* [18] values are shown in Fig. 18.

To assess the quality of the parameter optimization, the PDF flux was determined by the fitted model equation using the previously presented sets of fitting constraints. As an example of the fit quality at $x/h = 1.5$ and $y/h = 0.8$, i.e., the contraction slope, where the largest absolute mean acceleration is located, the resulting fluxes, and the actual flux obtained from the streamline statistics are compared in Fig. 19. The parameters for homogeneous turbulence result in a flux distribution which strongly differs from the actual flux. There is no coherent region of positive flux for either

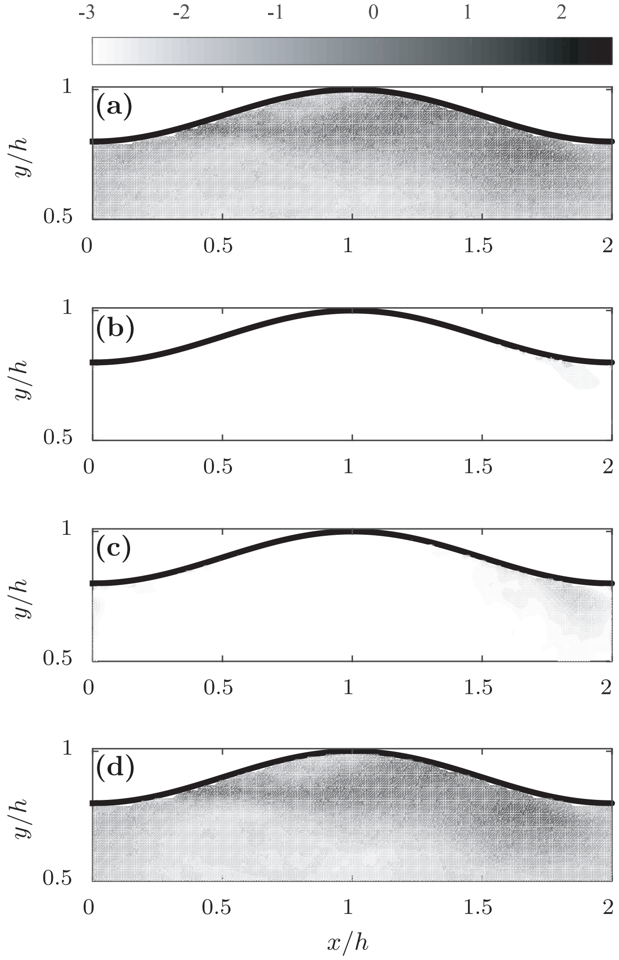

FIG. 18. Logarithm to base 10 of the parameter fitting residuals. (a) Parameters for homogeneous turbulence, (b) fully free fit, (c) $\widetilde{c_{l,\nu}}$ fixed at 0.5, and (d) $\widetilde{c_{\Delta,\nu}}$ fixed at 1.

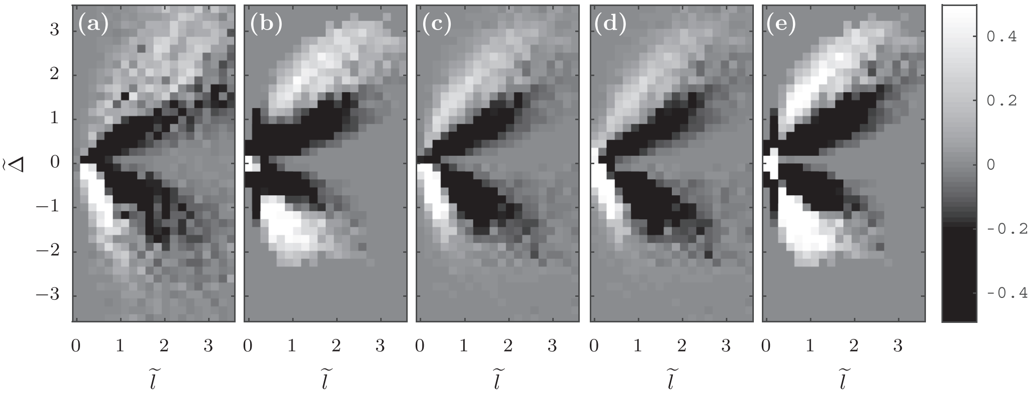

FIG. 19. Exemplary jPDF fluxes. (a) Fluxes based on statistics, (b) parameters for homogeneous turbulence, (c) fully free fit, (d) $\widetilde{c_{l,\nu}}$ fixed at 0.5, and (e) $\widetilde{c_{\Delta,\nu}}$ fixed at 1.

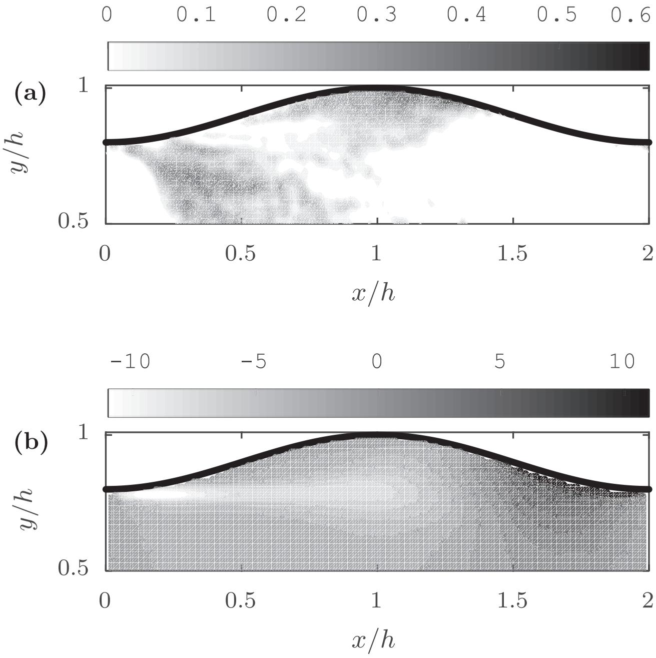

FIG. 20. Comparison of inner kinematics and background strain distributions (a) $\widetilde{C_\Delta}$-distribution (b) Background strain.

positive or negative inner velocity differences as found in the distribution obtained from the segment statistics. Instead, the flux of very short segments with small inner velocity difference assumes very high values surrounded by negative fluxes. Additionally, the fluxes of segments with large inner velocity differences present larger values than found in the statistics. A similar result is observed when only $\widetilde{c_{\Delta,\nu}}$ is set to a fixed value of one. Neither of these fluxes matches the statistics from the DNS data well, which agrees with the residuals found throughout the grid. The fully free fit and the fit with $\widetilde{c_{l,\nu}}$ set to 0.5 yield very similar distributions and magnitudes. Both fluxes do equally well approximate the actual flux based on the local statistics. This is hardly surprising given their very low residuals.

Based on the parameter distributions obtained with $\widetilde{c_{l,\nu}}$ at 0.5, other parameters can be analyzed. This case is chosen since it fits the statistical data equally well while presenting coherent regions in its parameter distributions which correlate with the mean velocity statistics. The first item of interest is the contribution of the streamline segment kinematics to the overall statistics. In work by Schäfer *et al.* [18], the characteristic asymmetry of the jPDF is a sole function of $\widetilde{C_\Delta}$, which represents the rate of change of the segments' lengths due to their inner velocity difference. However, its distribution in the wavy channel flow presents large regions where its value is approximately zero. Two notable exceptions can be observed in the trough region and the reattachment point in particular and in a fan-shaped region following the wave's upstream crest. Interestingly, the comparison with Fig. 20(b) shows two regions of moderate acceleration and therefore background strain. This suggests that this mechanism is dominated by the background strain in other regions. Additionally, in between those regions the expansion slope of the wave presents a distinct local area, in which $\widetilde{C_\Delta}$ approaches zero, while a large compressive background strain can be observed.

Concerning the evolution of the inner velocity differences due to the streamline segment kinematics, the corresponding timescales $\widetilde{\tau}^+$ and $\widetilde{\tau}^-$ are shown in Fig. 21. Similar to the distribution of $\widetilde{C_\Delta}$, in large portions of the flow the kinematics appear to be dominated by other effects since these nondimensional timescales show values beyond a million, rendering the impact of the

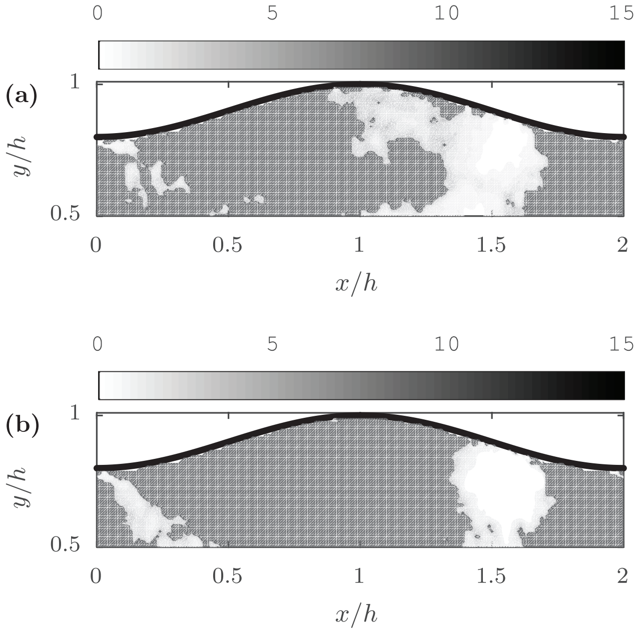

FIG. 21. Dimensionless timescales of inner kinematics (a) $\tilde{T}^+$-distribution (b) $\tilde{T}^-$-distribution.

kinematics negligible. However, in the regions with large values for $\widetilde{C_\Delta}$ such as the wave crest and the reattachment point, the timescales drop significantly, suggesting a larger contribution by the streamline segment kinematics. The region associated with the reattachment point extends well into the channel along the boundary between positive and negative background strain, spanning the narrow area of moderate strain.

In homogeneous turbulence, the fast processes balance the effects of the streamline kinematics and the diffusive contributions. The characteristic asymmetry in homogeneous turbulence is a simple balance between the inner kinematics and the cutting process. To maintain a statistically steady state, the occurrence rates of merging and cutting are required to assume a ratio of exactly two. Because of the convective flux, this is no longer the case in inhomogeneous turbulence, even though the previous considerations concerning the residuals suggest that an increased contribution of one process will result in other process activities being increased as well. The occurrence rates $\Lambda_c = \lambda_c \frac{l_m^2}{\sigma}$ and $\Lambda_a = \mu_a \frac{l_m}{\sigma}$ are shown in Fig. 22. The reattachment process occurs almost exclusively in the crest regions while the cutting process is most apparent along the shear layer of the separation bubble. Even though each fast process type can be considered the inverse process of the other, there is one major difference in their occurrence rates. While the occurrence of a reattachment event is equally likely for all segment classes, the cutting frequency is expressed as occurrence rate per segment length. Therefore, the expectancy value for the segment length of the segment created during a reattachment event is twice the mean segment length of the merging segment type. As a consequence, the reattachment process cannot change the asymmetry of the jPDF since both segment types equally grow in length. However, the cutting process is more likely to cut long segments which causes the longer segment type to be cut more often. Effectively, this process counteracts the asymmetry in any jPDF. The elevated levels of cutting rates in the shear layer and the separation region as shown in Fig. 22(a) indicate that this might in fact be the cause for the asymmetry to not scale with the background strain in such regions.

Lastly, the generic source term for velocity differences is investigated. The original formulation by Schäfer *et al.* [18] became necessary to reach a steady state in homogeneous turbulence by

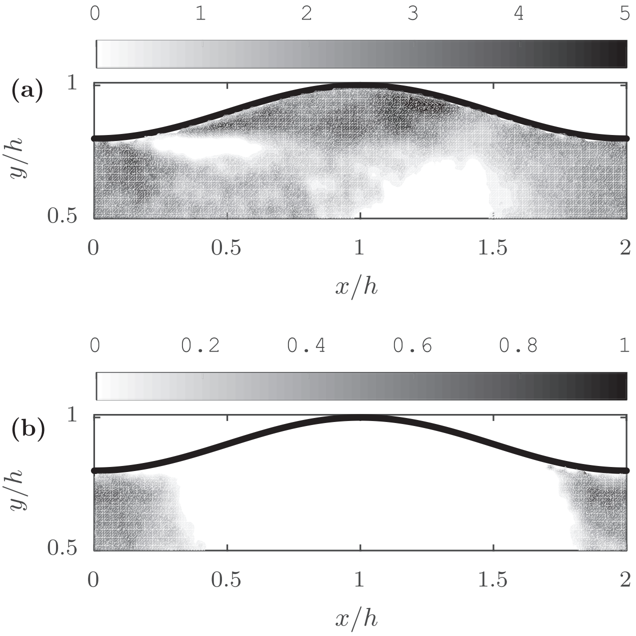

FIG. 22. Dimensionless occurrence rates of cutting and reattachment processes (a) Λ_c-distribution (b) Λ_a-distribution.

increasing or decreasing the overall level of velocity differences which otherwise would decay over time. As previously described, this source term of the form $\widetilde{K}\mathrm{sgn}(\Delta)$ is part of the velocity drift. However, this formulation assumes the source strength to be independent of the segment length. Under inhomogeneous conditions, this is hardly the case. At the contraction slope, the large mean acceleration will not only stretch passing structures but instead also modify the inner velocity difference since the leading portion of the structure will already undergo an acceleration before the remaining portion reaches this area. This effect will be more pronounced for large structures, which makes it reasonable to assume that the velocity difference source must scale with length. Therefore, the source term was modified to $\widetilde{K}^*\widetilde{l}$.

Note that this no longer forces the two segment types to experience opposite source effects since the sign of the inner velocity difference was removed. Consequently, the source strength now only scales with the segment length regardless of other factors. The parameter optimization was repeated for the adapted propagation equation with the modified source term. The residual of the modified case is very similar at the same level of the residual found for the original source term, indicating equally well-fitting solutions. The source strengths for parameters obtained with the original and adapted source terms are shown in Fig. 23. Note that the modified source strength in Fig. 23(b) presents a distribution roughly comparable to the background strain as shown in Fig. 20(b), indicating that the streamwise background strain can cause the fluctuations of the individual structures to grow or decay.

Overall, the results indicate a vastly changed behavior in comparison to homogeneous turbulence. The parameters obtained from the adapted model function undergo strong variations throughout the domain. Particularly the parameters associated with the kinematics of the streamline segments are dominated by the pressure-driven background strain in most regions. Nonetheless, the model parameters can indicate which processes are responsible for the observations from experiments.

To investigate the suitability of the novel formulation of the streamline statistics propagation equation for describing inhomogeneous flows, synthetic joint probability distributions were gen-

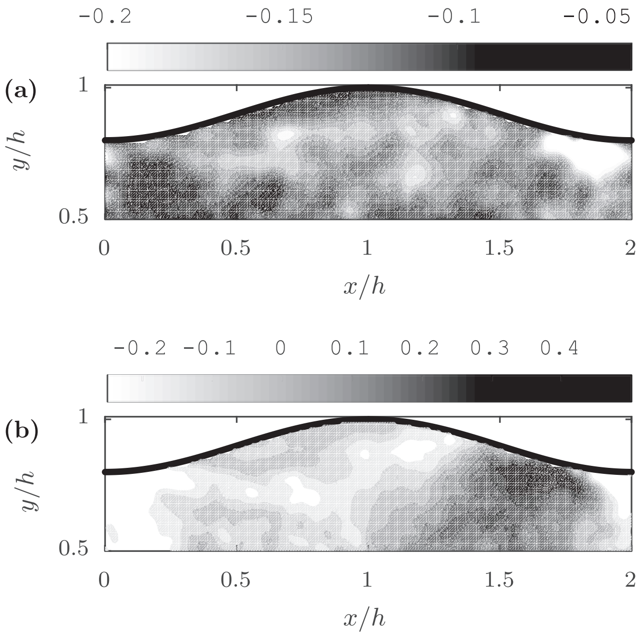

FIG. 23. Dimensionless source terms for the velocity difference within the segments (a) $\widetilde{K}$-distribution (b) $\widetilde{K}^{*}$-distribution.

erated based on the previously determined process parameters and convective structure fluxes. Different from the parameter optimization, the parameters are known now while the jPDF is unknown, resulting in a nonlinear optimization problem with 800 degrees of freedom, which corresponds to the resolution of the probability distribution. The residual is formulated as the squared sum of all convective structure flux differences between the values obtained from statistics and the values calculated from the synthetic jPDF and the model equation similarly to the process parameter optimization. Since some properties of the nondimensional jPDF of streamline segments are known [18], they are imposed as optimization constraints.

$$\int_0^\infty \int_{-\infty}^\infty P(\tilde{l}, \widetilde{\Delta})d\widetilde{\Delta}d\tilde{l} = 1, \quad \int_0^\infty \int_{-\infty}^\infty lP(\tilde{l}, \widetilde{\Delta})d\widetilde{\Delta}d\tilde{l} = 1, \quad \left(\int_0^\infty \int_{-\infty}^\infty \widetilde{\Delta}^2 P(\tilde{l}, \widetilde{\Delta})d\widetilde{\Delta}d\tilde{l}\right)^{\frac{1}{2}} = 1.$$

Additionally, the distribution approaches zero at all boundaries and at $\widetilde{\Delta} = 0$. Furthermore, since the streamline segment detection bias was accounted for and compensated such that the same number of positive and negative segments are included in the statistics, this can be used as an additional constraint:

$$\int_0^\infty \int_0^\infty P(\tilde{l}, \widetilde{\Delta})d\widetilde{\Delta}d\tilde{l} = \int_0^\infty \int_{-\infty}^0 P(\tilde{l}, \widetilde{\Delta})d\widetilde{\Delta}d\tilde{l}.$$

As the initial point for the optimization process, an entirely uniform distribution is selected. The nonlinear optimization process iteratively lowers the residual until it reaches a minimum. In the current case, this typically requires approximately 100 iterations resulting in nearly 100 000 evaluations of the residual. An exemplary synthetic jPDF and the actual jPDF obtained from statistics in the contraction slope region are shown in Fig. 24.

The two characteristic lobes of streamline segment jPDF are evident. While the synthetic distribution presents a somewhat more scattered Δ-wise shape, the asymmetry is quite comparable

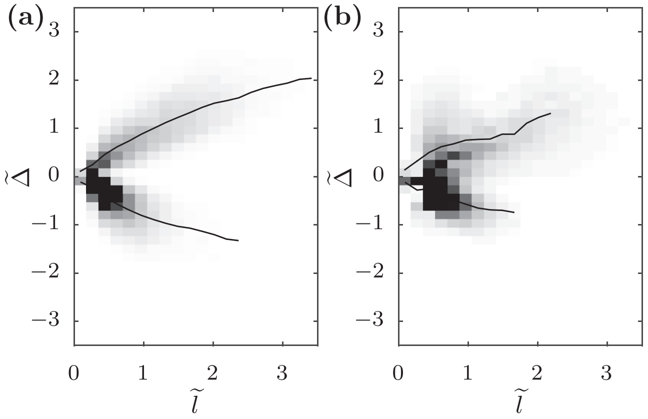

FIG. 24. Original (a) and synthetically generated jPDF (b) at $x/h = 1.5$ and $y/h = 0.8$.

to the real distribution since positive segments clearly exhibit a larger mean segment length than negative segments. The asymmetry characteristics can be compared using the mean inner velocity difference $\langle\widetilde{\Delta}\rangle$ and the mean segment length ratio $(l_m^+ - l_m^-)/l_m$. The average mean differences are quite comparable at 0.21 for streamline statistics and 0.197 for the synthetic distribution. The mean segment length ratios match well at 0.61 and 0.63. Considering the uncertainties due to the statistical noise affecting the model function parameters and the structure flux, the results can be viewed as a proof of concept that the novel formulation of the model equation can describe the propagation of streamline segment statistics in inhomogeneous flows.

IV. CONCLUSION AND DISCUSSION

The streamline segment statistics in a wavy channel flow is investigated by tomographic particle-image velocimetry and direct numerical simulations. The influence of the background strain on the statistics is confirmed. The selection of the observed region can introduce a bias in the detection of streamline segments. Because of the extended field of view in the current study, the impact of the background strain could be determined more accurately than in former investigations. However, the impact of the background strain on the streamline segments is not an immediate deformation of the probability distribution.

To gain further insight into the mechanism acting on the probability distribution, its propagation equation is adapted for inhomogeneous flow by proposing a locality definition, which is able to capture segments of all length classes without introducing a bias. Because of the added complexity under inhomogeneous conditions, the novel propagation equation accounts for the paradigms necessitated by the locality definition.

Using the newly adapted propagation equation, the various process parameters are fitted locally. Most notably, it is found that the point of detachment, the shear layer above the separation, and the reattachment point present strongly increased levels in their segment cutting frequency. The cutting mechanism severely limits the local statistical asymmetry by splitting long segments and therefore counteracting the effect of the background strain. This agrees well with the observations from tomographic PIV data, in which the asymmetry could not align with the near-wall background strain at attached flow since the elevated shear level encourages the cutting process and counteracts larger asymmetries. In terms of the propagation equation, the background strain can be used as a source term for the velocity drift.

Finally, because of their inner velocity difference the kinematics of streamline segments is one of the driving factors in equilibrium homogeneous turbulence. Under the current condition, the outcome of the analysis of the kinematics is emphasized in regions of near-zero background strain.

ACKNOWLEDGMENT

This work was funded by the Deutsche Forschungsgemeinschaft within the research project SCHR 309/41-2: ”Geometric Structure of Small Scale Turbulence.”

APPENDIX: PARAMETER FITTING PROCEDURE

The parameter fitting procedure is performed for each cell of the statistics grid individually on the following equation:

$$
\begin{aligned}
\left.\frac{d\widetilde{P}}{d\tau}\right|_{\text{conv}} &+ \underbrace{\frac{\partial}{\partial\widetilde{l}}[\widetilde{a_{1,l}}\widetilde{P}(\widetilde{l},\widetilde{\Delta})]}_{\textbf{I}} + \underbrace{\frac{\partial}{\partial\widetilde{\Delta}}[\widetilde{a_{1,\Delta}}\widetilde{P}(\widetilde{l},\widetilde{\Delta})]}_{\textbf{II}} \\
&= \Lambda_c \underbrace{\left(2\int_0^\infty\int_{\widetilde{l}}^\infty \delta\left(\psi k\left(\frac{\widetilde{l}}{y}\right)-\widetilde{\Delta}\right)\widetilde{P}(y,\psi)dyd\psi - \widetilde{l}\widetilde{P}(\widetilde{l},\widetilde{\Delta})\right)}_{\textbf{III}} \\
&+ 2\Lambda_a \underbrace{\left(\int_0^{\widetilde{\Delta}}\int_0^{\widetilde{l}} \frac{y}{\widetilde{l}}\widetilde{P}(\widetilde{l}-y,\widetilde{\Delta}-\psi)\widetilde{P}(y,\psi)dyd\psi - \widetilde{P}(\widetilde{l},\widetilde{\Delta})\right)}_{\textbf{IV}}.
\end{aligned}
$$

Based on the locality definition proposed in Sec. III C, all segments associated with a particular cell are identified and the parameters l_m and σ can be determined. Based on these parameters, the normalized jPDF can be determined for each cell. To compensate for the detection bias of one segment type depending on the asymmetry, the jPDF is rebalanced as described in Sec. III C:

$$
\int_0^\infty\int_0^\infty \widetilde{P}(y,\psi)dyd\psi = \int_0^\infty\int_{-\infty}^0 \widetilde{P}(y,\psi)dyd\psi = \frac{1}{2}.
$$

The spatial derivatives of the l_m, σ, and $\widetilde{P}(\widetilde{l},\widetilde{\Delta})$ fields can now be obtained by a simple linear fit of all immediately adjacent cells. These quantities allow for the evaluation of $\frac{d\widetilde{P}}{d\tau}|_{\text{conv}}$ for each bin of the jPDF.

The drift terms can be split into expressions with the model parameters as leading coefficients while the cutting and reattachment terms already present this form:

$$
\mathrm{I} = \widetilde{c_{l,\nu}}\underbrace{\frac{\partial}{\partial\widetilde{l}}\left(\left\{\frac{c_s}{\widetilde{l}}[1-\exp(-2\widetilde{l})]-\frac{1}{\widetilde{l}}\right\}\widetilde{P}(\widetilde{l},\widetilde{\Delta})\right)}_{I_A} + \widetilde{C_\Delta}\underbrace{\frac{\partial}{\partial\widetilde{l}}[\widetilde{\Delta}\widetilde{P}(\widetilde{l},\widetilde{\Delta})]}_{I_B}
$$

$$
\mathrm{II} = \widetilde{c_{\Delta,\nu}}\underbrace{\frac{\partial}{\partial\widetilde{\Delta}}\left[-\frac{\widetilde{\Delta}}{\widetilde{l}^2}\exp(-3\widetilde{l})\widetilde{P}(\widetilde{l},\widetilde{\Delta})\right]}_{II_A} + \widetilde{K}\underbrace{\frac{\partial}{\partial\widetilde{\Delta}}[\mathrm{sgn}(\widetilde{\Delta})\widetilde{P}(\widetilde{l},\widetilde{\Delta})]}_{II_B} + \frac{1}{\widetilde{\tau^{+,-}}}\underbrace{\frac{\partial}{\partial\widetilde{\Delta}}[\widetilde{\Delta}\widetilde{P}(\widetilde{l},\widetilde{\Delta})]}_{II_C}.
$$

Finally, a linear system, in which each row represents one of N bins of the jPDF, can formulated and solved for the local parameters. Each bin represents a certain combination of $\widetilde{l}$ and $\widetilde{\Delta}$. To be able to detect $\widetilde{\tau^+}$ and $\widetilde{\tau^-}$ separately, the term II_C is duplicated. The matrix entries marked with an asterisk (*) assume the value 0 when $\widetilde{\Delta}$ is smaller than 0. The opposite is true for the term labeled with two asterisks (**):

$$\begin{pmatrix} -I_A^1 & -I_A^2 & \dots & -I_A^N \\ -I_B^1 & -I_B^2 & \dots & -I_B^N \\ -II_A^1 & -II_A^2 & \dots & -II_A^N \\ -II_B^1 & -II_B^2 & \dots & -II_B^N \\ -II_C^{*,1} & -II_C^{*,2} & \dots & -II_C^{*,N} \\ -II_C^{**,1} & -II_C^{**,2} & \dots & -II_C^{**,N} \\ III^1 & III^2 & \dots & III^N \\ IV^1 & IV^2 & \dots & IV^N \end{pmatrix}^T \cdot \begin{pmatrix} \widetilde{c_{l,\nu}} \\ \widetilde{C_\Delta} \\ \widetilde{c_{\Delta,\nu}} \\ \widetilde{K} \\ \frac{1}{\widetilde{\tau^+}} \\ \frac{1}{\widetilde{\tau^-}} \\ \Lambda_c \\ \Lambda_a \end{pmatrix} = \begin{pmatrix} \frac{d\widetilde{P}}{d\tau}\Big|^1_{\text{conv}} \\ \frac{d\widetilde{P}}{d\tau}\Big|^2_{\text{conv}} \\ \vdots \\ \frac{d\widetilde{P}}{d\tau}\Big|^N_{\text{conv}} \end{pmatrix}.$$

[1] A. Tsinober, *An Informal Introduction to Turbulence*, Fluid Mechanics and Its Applications (Springer, Dordrecht, 2001).

[2] D. Tritton, *Physical Fluid Dynamics*, Oxford Science Publications (Clarendon Press, Oxford, 1988).

[3] S. Corrsin, Random geometric problems suggested by turbulence, in *Statistical Models and Turbulence* (Springer, Berlin, 1972), pp. 300–316.

[4] J. C. R. Hunt, A. A. Wray, and P. Moin, Eddies, stream, and convergence zones in turbulent flows, in *Studying Turbulence Using Numerical Simulation Databases, 2* (NASA/STI, Washington, DC, 1988), pp. 193–208.

[5] L. Richardson and P. Lynch, *Weather Prediction by Numerical Process*, Cambridge Mathematical Library (Cambridge University Press, Cambridge, UK, 2007).

[6] G. Haller, An objective definition of a vortex, J. Fluid Mech. **525**, 1 (2005).

[7] G. Ruetsch and M. Maxey, Small-scale features of vorticity and passive scalar fields in homogeneous isotropic turbulence, Phys. Fluids A **3**, 1587 (1991).

[8] D. Pullin and P. Saffman, Vortex dynamics in turbulence, Annu. Rev. Fluid Mech. **30**, 31 (1998).

[9] N. Peters and L. Wang, Dissipation element analysis of scalar fields in turbulence, Compt. Rend. Mécan. **334**, 493 (2006).

[10] L. Wang and N. Peters, Length-scale distribution functions and conditional means for various fields in turbulence, J. Fluid Mech. **608**, 113 (2008).

[11] F. Aldudak and M. Oberlack, Dissipation element analysis in turbulent channel flow, J. Fluid Mech. **694**, 332 (2012).

[12] L. Schäfer, U. Dierksheide, M. Klaas, and W. Schröder, Investigation of dissipation elements in a fully developed turbulent channel flow by tomographic particle-image velocimetry, Phys. Fluids **23**, 035106 (2011).

[13] L. Schäfer, J. H. Göbbert, and W. Schröder, Dissipation element analysis in experimental and numerical shear flow, Eur. J. Mech., B **38**, 85 (2013).

[14] P. Schäfer, M. Gampert, J. H. Goebbert, L. Wang, and N. Peters, Testing of model equations for the mean dissipation using kolmogorov flows, Flow, Turbulence Combust. **85**, 225 (2010).

[15] L. Wang, On properties of fluid turbulence along streamlines, J. Fluid Mech. **648**, 183 (2010).

[16] P. Schäfer, M. Gampert, and N. Peters, The length distribution of streamline segments in homogeneous isotropic decaying turbulence, Phys. Fluids **24**, 045104 (2012).

[17] P. Schäfer, M. Gampert, and N. Peters, On the scaling of the mean length of streamline segments in various turbulent flows, Comp. Rend. Mécan. **340**, 859 (2012).

[18] P. Schäfer, M. Gampert, and N. Peters, A model equation for the joint distribution of the length and velocity difference of streamline segments in turbulent flows, Phys. Fluids **25**, 115107 (2013).

[19] A. Rubbert, F. Hennig, M. Klaas, H. Pitsch, W. Schröder, and N. Peters, Streamline segment scaling behavior in a turbulent wavy channel flow, Exp. Fluids **58**, 10 (2017).

[20] D. P. Zilker and T. J. Hanratty, Influence of the amplitude of a solid wavy wall on a turbulent flow. Part 2. Separated flows, J. Fluid Mech. **90**, 257 (1979).

[21] P. Cherukat, Y. Na, T. Hanratty, and J. McLaughlin, Direct numerical simulation of a fully developed turbulent flow over a wavy wall, Theor. Comput. Fluid Dyn. **11**, 109 (1998).

[22] R. Moser, J. Kim, and N. Mansour, Direct numerical simulation of turbulent channel flow up to $re_\tau = 590$, Phys. Fluids **11**, 943 (1999).

[23] C. Atkinson and J. Soria, An efficient simultaneous reconstruction technique for tomographic particle image velocimetry, Exp. Fluids **47**, 553 (2009).

[24] S. Discetti and T. Astarita, Fast 3d PIV with direct sparse cross-correlations, Exp. Fluids **53**, 1437 (2012).

[25] M. Novara, K. J. Batenburg, and F. Scarano, Motion tracking-enhanced mart for tomographic PIV, Meas. Sci. Technol. **21**, 035401 (2010).

[26] M. Meinke, W. Schröder, E. Krause, and T. Rister, A comparison of second- and sixth-order methods for large-eddy simulations, Comput. Fluids **31**, 695 (2002).

[27] F. Hennig, J. Boschung, and N. Peters, *Statistical Description of Streamline Segments in a Turbulent Channel Flow with a Wavy Wall* (Springer International, Cham, 2016), pp. 135–143.

[28] L. Wang and N. Peters, The length-scale distribution function of the distance between extremal points in passive scalar turbulence, J. Fluid Mech. **554**, 457 (2006).